Magnetoresistance of nanoscale molecular devices based on Aharonov-Bohm interferometry

2008 J. Phys.: Condens. Matter 20 383201

(http://iopscience.iop.org/0953-8984/20/38/383201)

IOP PUBLISHING JOURNAL OF PHYSICS: CONDENSED MATTER

J. Phys.: Condens. Matter **20** (2008) 383201 (32pp) doi:10.1088/0953-8984/20/38/383201

TOPICAL REVIEW

Magnetoresistance of nanoscale molecular devices based on Aharonov–Bohm interferometry

Oded Hod[1], **Roi Baer**[2] **and Eran Rabani**[3]

[1] Department of Chemistry, Rice University, Houston, TX 77005-1892, USA
[2] Institute of Chemistry, and the Fritz Haber Center for Molecular Dynamics, The Hebrew University of Jerusalem, Jerusalem 91904, Israel
[3] School of Chemistry, The Sackler Faculty of Exact Sciences, Tel Aviv University, Tel Aviv 69978, Israel

E-mail: oded.hod@rice.edu, roi.baer@huji.ac.il and rabani@tau.ac.il

Received 17 January 2008, in final form 11 July 2008
Published 27 August 2008
Online at stacks.iop.org/JPhysCM/20/383201

Abstract

Control of conductance in molecular junctions is of key importance in the growing field of molecular electronics. The current in these junctions is often controlled by an electric gate designed to shift conductance peaks into the low bias regime. Magnetic fields, on the other hand, have rarely been used due to the small magnetic flux captured by molecular conductors (an exception is the Kondo effect in single-molecule transistors). This is in contrast to a related field, electronic transport through mesoscopic devices, where considerable activity with magnetic fields has led to a rich description of transport. The scarcity of experimental activity is due to the belief that significant magnetic response is obtained only when the magnetic flux is of the order of the quantum flux, while attaining such a flux for molecular and nanoscale devices requires unrealistic magnetic fields.

Here we review recent theoretical work regarding the essential physical requirements necessary for the construction of nanometer-scale magnetoresistance devices based on an Aharonov–Bohm molecular interferometer. We show that control of the conductance properties using small fractions of a magnetic flux can be achieved by carefully adjusting the lifetime of the conducting electrons through a pre-selected single state that is well separated from other states due to quantum confinement effects. Using a simple analytical model and more elaborate atomistic calculations we demonstrate that magnetic fields which give rise to a magnetic flux comparable to 10^{-3} of the quantum flux can be used to switch a class of different molecular and nanometer rings, ranging from quantum corrals, carbon nanotubes and even a molecular ring composed of polyconjugated aromatic materials.

The unique characteristics of the magnetic field as a gate is further discussed and demonstrated in two different directions. First, a three-terminal molecular router devices that can function as a parallel logic gate, processing two logic operations simultaneously, is presented. Second, the role of inelastic effects arising from electron–phonon couplings on the magnetoresistance properties is analyzed. We show that a remarkable difference between electric and magnetic gating is also revealed when inelastic effects become significant. The inelastic broadening of response curves to electric gates is replaced by a narrowing of magnetoconductance peaks, thereby enhancing the sensitivity of the device.

(Some figures in this article are in colour only in the electronic version)

Contents

1. Introduction

In the past two decades molecular electronics has emerged as one of the most active and intriguing research fields [1–23]. Scientifically, this field offers insights into fundamental issues regarding the physics of low-dimensional and nanometer-scale systems as well as their response to external perturbations when embedded in complicated environments. From a technological point of view, electronic functionality at the molecular scale may revolutionize our current conception of electronic devices and may lead to considerable miniaturization of their dimensions [1, 13]. Interestingly, the paradigm of molecular electronics was set by a theoretical study long before the first experimental realization was presented [24]. In their seminal work, Aviram and Ratner suggested that a donor–bridge–acceptor type of molecule could, in principle, act as a molecular rectifier. What designates this study is the fact that for the first time a *single molecule* was considered to act as an *electronic component* rather than just being a charge transfer medium. Therefore, it could serve as a potential building block for future nanoscale electronic devices [6, 7, 13, 16, 22].

In recent years, a number of experimental techniques have been developed for the synthesis and fabrication of junctions that allow for the measurement of the electronic transport through molecular-scale systems. These include mechanically controllable break junctions [25–28], electromigration break junctions [29–32], electron beam lithography [33, 34], feedback-controlled lithography [35], shadow evaporation [36, 37], electrochemical deposition [38–40], mercury droplet technologies [41–43], cross-wire tunnel junctions [44], STM [45, 46] and conducting AFM [47] tip measurements, and more [48–50]. In typical molecular electronics experiments, a molecule (or a group of molecules) is trapped within a gap between the electrodes while chemically or physically attaching to the conducting leads. Once the molecular junction is obtained, a bias voltage is applied and the current/voltage characteristics are recorded and analyzed. Certain techniques can also utilize an electrical or chemical gate electrode in order to control the response of the molecule to the applied bias [51–58, 34, 59–68]. A simplified picture of the effect of the gate voltage can be viewed as a shift in the energy of the molecular states of the device with respect to the Fermi energy of the conducting leads, allowing for fine tuning of the conductance through pre-selected molecular energy states.

Unlike the common use of electrical gates as control knobs for the transport characteristics of molecular junctions, magnetic fields have rarely been used in conjunction with molecular electronics. This is in contrast to a related field, electronic transport through mesoscopic systems, where considerable activity with magnetic fields has led to the discovery of the quantum Hall effect [69] and to a rich description of Aharonov–Bohm [70–87] magneto-transport phenomena in such conductors [88–100].

The scarcity of experimental activity involving magnetic fields in molecular electronic set-ups is due to the belief that a significant magnetic response is obtained only when the magnetic flux is of the order of the *quantum flux*, $\phi_0 = h/q_e$ (q_e being the electron charge and h Planck's constant) and attaining such a flux for molecular and nanoscale devices requires unrealistically huge magnetic fields. Nevertheless, several interesting experimental studies on the effect of magnetic fields in nanoscale systems have been published recently. The major part of these regard Zeeman splitting of spin states in quantum dots [101] and in carbon nanotubes [48, 102, 103], the Kondo effect measured for mesoscale quantum dots [104, 105], fullerenes [106–109], and single molecules [30, 34], and the quantum Hall effect in graphene nanoribbons [110].

In this review we discuss recent theoretical work utilizing magnetic fields as gates in molecular Aharonov–Bohm interferometers [111–115]. We show how the combination of electric and magnetic fields provide additional control over the electrical current. The unique symmetry breaking nature of the magnetic field allows for the design of novel logical devices such as multi-terminal electron routers [113] which are not feasible when electrical gating is applied alone. We also show that, when inelastic scattering effects are taken into account, a remarkable difference between electric and magnetic gating is revealed [114]. The inelastic broadening of response curves to electric gates is replaced by narrowing of magnetoconductance peaks, thereby enhancing the sensitivity of the device.

This review starts with a brief introduction to the Aharonov–Bohm (AB) effect and its feasibility in nanoscale systems (section 2). The basic concepts are described in section 3 for two- and three-terminal devices. The analysis of these AB interferometers is based on adopting a simple

continuum model. Next, in section 4 we described detailed atomistic calculations motivated by the results of the simple continuum approach. We illustrate that molecular AB interferometers based on a variety of systems can be used as switching devices at relatively low magnetic fields. We also illustrate a parallel molecular logic gate based on a three-terminal device. Finally, we describe the effect of inelastic scattering on the behavior of the molecular AB interferometers in section 5. Conclusions and a brief summary are given in section 6.

2. Defining open questions

2.1. Aharonov–Bohm interferometry

In classical mechanics the force exerted on a charged particle traversing a region in space which incorporates an electric and/or a magnetic field is given by the Lorentz force law $\mathbf{F} = q(\mathbf{E} + \mathbf{v} \times \mathbf{B})$, where q is the charge of the particle, $\mathbf{E}$ is the electric field, $\mathbf{v}$ is the particle's velocity and $\mathbf{B}$ is the magnetic field [116]. It can be seen that the electric field operates on a particle whether static or not and contributes a force parallel to its direction and proportional to its magnitude, while the magnetic field operates only on moving particles and contributes a force acting perpendicular to its direction and to the direction of the particle's movement. When solving Newton's equation of motion $\mathbf{F} = \frac{\mathrm{d}\mathbf{P}}{\mathrm{d}t}$, the resulting trajectories for a classical charged particle entering a region of a uniform magnetic field will thus be circular. One can define scalar and vectorial potentials using the following definitions: $\mathbf{E}(\mathbf{r}, t) = -\nabla V - \frac{\partial \mathbf{A}(\mathbf{r},t)}{\partial t}$ and $\mathbf{B}(\mathbf{r}, t) = \nabla \times \mathbf{A}(\mathbf{r}, t)$, respectively. When defining the following Lagrangian $L = \frac{1}{2}m\mathbf{v}^2 - qV(\mathbf{r}) + q\mathbf{v}\cdot\mathbf{A}$, and deriving the canonical momentum using the relation $\mathbf{P}_i = \frac{\partial L}{\partial \dot{\mathbf{r}}_i}$ one can, in principle, solve the Euler–Lagrange or Hamilton equations of motion. This procedure, even though easier to solve for some physical problems, is absolutely equivalent to solving Newton's equations of motion and will produce the exact same trajectories.

The influence of electric and magnetic fields on the dynamics of quantum charged particles was investigated by Aharonov and Bohm in a seminal work from 1959 [71], revealing one of the fundamental differences between the classical and the quantum description of nature. According to Aharonov and Bohm, while in classical mechanics the transition from using electric and magnetic fields to using scalar and vectorial potentials is 'cosmetic' and may be regarded as a mathematical pathway for solving equivalent problems, in quantum mechanics the fundamental quantities are the potentials themselves.

In order to demonstrate this principle consider a double-slit experiment applied to electrons. The experimental set-up consists of a source emitting coherent electrons which are diffracted through two slits embedded in a screen. The electron intensity is measured in a detector placed on the opposite side of the screen. In the absence of a magnetic field the intensity measured by the detector when placed directly opposite to the source will be maximal due to the positive interference between the two electron pathways which are of equal length.

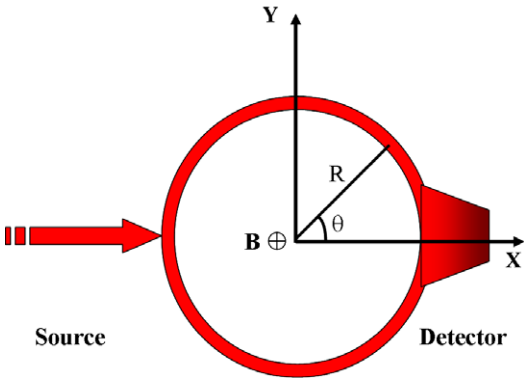

Figure 1. An Aharonov–Bohm ring-shaped interferometer connecting a coherent electron source and a detector.

When applying a point magnetic field perpendicular to the interference plane, the interference intensity is altered. Unlike the classical prediction, this change in the interference pattern is expected even if the magnetic field is excluded from both electron pathways. This can be traced back to the fact that, even though the magnetic field is zero along these pathways, the corresponding vector potential does not necessarily vanish at these regions.

A more quantitative description of this phenomenon can be obtained by considering an analogous model consisting of a ring-shaped ballistic conductor forcing the bound electrons to move in a circular motion connecting the source and the detector as shown in figure 1. The Hamiltonian of the electrons under the influence of electric and magnetic potentials is given by

$$\hat{H} = \frac{1}{2m}\left[\hat{\mathbf{P}} - q\mathbf{A}(\hat{\mathbf{r}})\right]^2 + \hat{V}(\hat{\mathbf{r}}). \tag{1}$$

Field quantization is disregarded in the entire treatment and we assume that the potentials are time-independent. In the above, m is the mass of the particle, $\hat{\mathbf{P}} = -\mathrm{i}\hbar\hat{\nabla}$ is the canonical momentum operator and $\hbar$ is Planck's constant divided by 2π. In the absence of electrostatic interactions, the Hamiltonian reduces to the free particle Hamiltonian with the appropriate kinetic momentum operator $\hat{\tilde{\mathbf{P}}} = \hat{\mathbf{P}} - q\mathbf{A}(\hat{\mathbf{r}})$.

In the set-up shown in figure 1 the wavefunction splits into two distinct parts, one traveling through the upper arm and the other through the lower arm of the ring. Since the magnetic field is excluded from these paths ($\nabla \times \mathbf{A} = 0$) and both are simply connected in space, it is possible to write a solution to the stationary Schrödinger equation with this Hamiltonian at each path as follows:

$$\Psi^{u/d} = \mathrm{e}^{\mathrm{i}\int_{u/d}(\mathbf{k} - \frac{q}{\hbar}\mathbf{A})\cdot\mathbf{dl}}, \tag{2}$$

where $\mathbf{k}$ is the wavevector of the charged particle and the integration is taken along its pathway, with u/d standing for the upper (up) and lower (down) pathways, respectively. Due to the circular symmetry of the system, the spatial phase factors accumulated along the upper or the lower branches of the ring can be easily calculated in the following manner:

$$\Phi_k = \int_{\pi}^{0} \mathbf{k}\cdot\mathbf{dl} = \pi Rk. \tag{3}$$

Here $\mathbf{k}$ is taken to be along the ring and $k = |\mathbf{k}|$ is the wavenumber of the electron. When a uniform[4] magnetic field is applied perpendicular to the cross section of the ring, $\mathbf{B} = (0, 0, B_z)$, the vector potential may be written as $\mathbf{A} = -\frac{1}{2}\mathbf{r} \times \mathbf{B} = \frac{1}{2}B_z(-y, x, 0) = \frac{RB_z}{2}(-\sin(\theta), \cos(\theta), 0)$. Thus, the magnetic phase accumulated by the electron while traveling from the source to the detector in a clockwise manner through the upper path is given by

$$\Phi_m^u = -\frac{q}{\hbar}\int_{\pi}^{0} \mathbf{A}\cdot\mathbf{dl} = \pi\frac{\phi}{\phi_0}. \tag{4}$$

Here, $\phi = B_z S$ is the magnetic flux threading the ring, $\phi_0 = \frac{h}{q}$ is the flux quantum and $S = \pi R^2$ is the cross-sectional area of the ring. For an electron traveling through the lower path in a counterclockwise manner the magnetic phase has the same magnitude with an opposite sign:

$$\Phi_m^l = -\frac{q}{\hbar}\int_{\pi}^{2\pi} \mathbf{A}\cdot\mathbf{dl} = -\pi\frac{\phi}{\phi_0}. \tag{5}$$

The electron intensity measured at the detector is proportional to the square absolute value of the sum of the upper and lower wavefunction contributions:

$$I \propto \left|\Psi^u + \Psi^d\right|^2 = \left|e^{i\pi\left(Rk+\frac{\phi}{\phi_0}\right)} + e^{i\pi\left(Rk-\frac{\phi}{\phi_0}\right)}\right|^2$$
$$= 2\left[1+\cos\left(2\pi\frac{\phi}{\phi_0}\right)\right]. \tag{6}$$

The intensity measured at the detector is, therefore, a periodic function of the magnetic flux threading the ring's cross section. As mentioned before, this general and important result holds also when the magnetic field is not applied uniformly and measurable intensity changes may be observed at the detector even if the applied magnetic field is excluded from the circumference of the ring to which the electrons are bound.

2.2. Length scales

The model described above presents an idealized system for which the charge carrying particles travel from the source to the detector without losing either momentum or phase. When considering the issue of measuring the AB effect in a realistic system, a delicate balance between three important length scales is needed: (a) the Fermi wavelength, (b) the mean free path and (c) the coherence length scale. In what follows, we shall give a brief description of each of these length scales and their importance for transport.

[4] The calculation given here assumes a uniform magnetic field even though it was claimed that equation (2) holds only in regions in space where $\mathbf{B} = 0$. Nevertheless, due to the fact that the electrons are confined to move on the one-dimensional ring, there is no essential difference between the case of a singular magnetic field and a homogeneous magnetic field. Therefore, the usage of the phases calculated here in equation (6) is valid. Furthermore, it should be noted that, due to Stokes' law, the line integration of $\mathbf{A}$ over a closed loop will always give the magnetic flux threading the ring whether the field is uniform, singular or of any other form.

2.2.1. Fermi wavelength. As in the optical double-slit experiment, the wavelength of the conducting electrons determines the interference intensity measured at the detector. At low temperatures and bias voltages the net current is carried by electrons in the vicinity of the Fermi energy and thus by controlling their wavelength one can determine whether positive or negative interference will be measured at the detector in the absence of a magnetic field.

In order to achieve positive interference, an integer number of Fermi wavelengths should fit into half the circumference of the ring [117, 115] (figure 1): $L = n\lambda_F$. Here, n is an integer, $L = \pi R$ is half of the circumference of the ring and λ_F is the Fermi electron's wavelength given by the well-known de Broglie relation $\lambda_F = \frac{h}{P_F} = \frac{2\pi}{k_F}$, where P_F is the momentum of the Fermi electrons and k_F is the associated wavenumber. For such a condition to be experimentally accessible, the Fermi wavelength should be approximately of the order of magnitude of the device dimensions. Too short wavelengths will give rise to extreme sensitivity of the interference pattern on the Fermi wavenumber, while too long wavelengths will show very low sensitivity. We shall return to the importance of controlling the wavelength of the conducting electrons in realistic systems measurements in sections 3.1 and 4.5.

2.2.2. Momentum relaxation length—static scatterers. An electron traveling in a perfect crystal can be viewed as a free particle with a renormalized mass [118]. This mass, which is usually referred to as the effective mass of the electrons in the crystal, incorporates the net effect of the periodic nuclei array on the conducting electrons. When impurities or defects exist in the crystalline structure the electrons may scatter on them. Such scattering implies a random change in the electron's momentum and thus destroys the ballistic nature of the conductance [119, 120]. The mean free path for momentum relaxation, L_m, is the average distance an electron travels before its momentum is randomized due to a collision with an impurity. It is typically connected to the momentum of the conducting electrons ($\hbar k_F$), their effective mass m^* and the collision time (τ, which is connected to the imaginary part of the self-energy of the quasiparticle): $L_m = \frac{\hbar k_F}{m^*}\tau$.

If the scattering taking place at the impurities sites is elastic, such that the energy of the electron and the magnitude of its momentum are conserved and only the direction of the momentum is randomized, then for a given trajectory a stationary interference pattern will be observed. However, different electron trajectories will give rise to different interference intensities and the overall interference pattern will not be stationary and thus will be averaged to zero [119].

2.2.3. Phase relaxation length—fluctuating scatterers. Inelastic scattering may occur when the impurities have internal degrees of freedom, which may exchange energy with the scattered electrons. Such scattering events alter the phase of the conducting electron. AB interferometry requires that a constant phase difference exists between the trajectories of electrons moving in the upper and the lower

arms of the interferometer ring. Thus, for stationary inelastic scatterers which shift the phase of the electrons in a persistent manner, a constant interference pattern will be measured at the detector. Although the intensity at zero magnetic field will not necessarily be at its maximal value, AB oscillations will be observed [119]. When the scatterers are not stationary, and the phase shifts they induce are not correlated between the two arms of the ring, the coherent nature of the conductance is destroyed and the AB interference pattern is diminished [119]. A length scale, L_ϕ, is assigned to this process and its physical meaning is that length electrons travel before they lose their phase. Apart from impurities, inelastic scattering may occur due to electron–phonon processes and electron–electron interactions. The latter conserve the total energy but allow energy exchange and thus phase randomization.

2.2.4. Regimes of transport. There are several different regimes for transport, depending on the values of the above length scales. If we denote the length of molecular device by L, then the ballistic regime is achieved when $L \ll L_\mathrm{m}, L_\phi$. When $L_\mathrm{m} \ll L \ll L_\phi$ the transport is diffusive and is reduced relative to the ballistic regime. Localization occurs when $L_\mathrm{m} \ll L_\phi \ll L$ and when the device is larger than both L_m and L_ϕ the system is considered to be classical with ohmic resistance.

2.3. Open questions

The design of a realistic AB interferometer requires a careful consideration of the typical length scales of the conducting electrons. In order to measure a significant AB periodicity it is necessary to reduce the dimensions of the interferometer below the momentum and phase relaxation lengths, and make it comparable to the de Broglie wavelength.

As an example, consider a ring made of GaAs/AlGaAs-based two-dimensional electron gas. The typical de Broglie wavelength is of the order of ∼30 nm, the mean free path (momentum relaxation length scale) is three orders of magnitude larger (∼30 μm) and the phase relaxation length is ∼1 μm [119]. Thus, one can expect to observe AB oscillations in the conductivity in loops with dimensions that are smaller than ≈1 μm with an AB period in the range of millitesla: $\frac{h}{q\pi R^2} \approx 1 \times 10^{-3}$ T [117].

For molecular rings these scales are quite different. The typical de Broglie wavelength is of the order of several chemical bonds (sub-nanometer) [111], while the mean free path of electrons and phase relaxation length are considerably larger than the dimensions of the ring. Thus, molecular AB interferometers at the nanometer scale are expected to show many AB oscillations, as long as the temperature is low enough so that inelastic effects arising from electron–phonon couplings are suppressed. However, in addition to the engineering challenge of fabricating such small and accurate devices, another substantial physical limitation becomes a major obstacle. When considering a nanometer-sized AB loop the period of the magnetic interference oscillations increases considerably and becomes comparable to $\frac{h}{q\pi R^2} \approx 1 \times 10^3$ T. Magnetic fields of these orders of magnitude are, by far, not accessible experimentally and thus AB interferometry is not expected to be measured for systems of small dimensions, at the nanometer scale.

In view of the above, several open questions arise:

(i) Can nanometric electronic devices based on an AB interferometer be made despite the large magnetic field required to complete a full AB period?
(ii) If such devices can be made, what are their physical properties? At what range of parameters (temperature, contact coupling, dimensions, etc) will they be able to operate?
(iii) What are the advantages/disadvantages of such magnetically gated devices over conventional electric gating?

In the remainder of this review we attempt to provide answers to the above problems. Despite the fact that the treatment described herein is theoretical, we believe that future technology will enable the development of realistic devices based on the concepts present below.

3. Basic concepts

In this section we describe the basic concepts of Aharonov–Bohm interferometry at the nanometer molecular scale. We consider two- and three-terminal devices. Transport is modeled within a simple continuum model that has been considered in mesoscopic physics for a two-terminal device only [89, 121, 90–92, 95, 122, 119, 123]. An exact solution for the conduction in both cases and analysis of the role of different model parameters is described. The two-terminal device is used to establish the necessary condition for switching a molecular Aharonov–Bohm interferometer at reasonably small magnetic fields, while the three-terminal device is used to demonstrate one of the advantages of magnetic gating in molecular AB interferometers.

3.1. Two-terminal devices

Consider a simple continuum model of an AB interferometer [89, 121, 90–92, 95, 122, 119, 123, 124]. The model consists of a one-dimensional (1D) single-mode conducting ring coupled to two 1D single-mode conducting leads as depicted in figure 2. The transport is considered to be ballistic along the conducting lines. Elastic scattering occurs at the two junctions only. Even though this model disregards the detailed electronic structure of the molecular device and neglects important effects, such as electron–electron interactions and electron–phonon coupling, it succeeds in capturing the important physical features needed to control the profile of the AB period.

The main feature differing the current arrangement from the one shown in figure 1 is that an 'outgoing' lead replaces the absorbing detector. Hence, the interference intensity measured at the detector is replaced by a measurement of the conductance between the two leads through the ring. Although it might seem insignificant, this difference is actually the heart of the approach developed to control the shape of the AB period. In the original setting, an electron arriving at the detector is immediately absorbed and therefore the intensity measured is

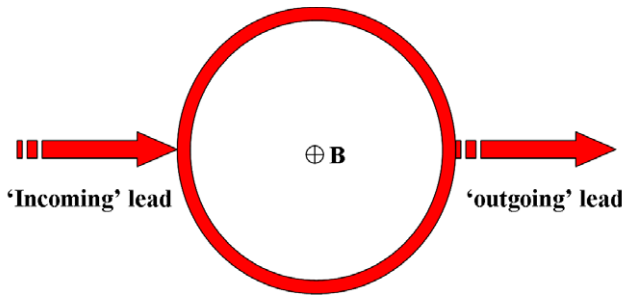

Figure 2. An illustration of a 1D coherent transport continuum model of an AB interferometer.

the outcome of the interference of the two distinct pathways the electron can travel. For the set-up considered in figure 2 an electron approaching each of the junctions can be either transmitted into the corresponding lead or be reflected back into one of the arms of the ring. Consequently, the conductance through the device is a result of the interference of an infinite series of pathways resulting from multiple scattering events of the electron at the junctions. It is obvious that the behavior predicted by equation (6) has to be modified to account for the interference between all pathways.

A scattering matrix approach [121, 92, 122, 119, 123, 125, 126] can now be used in order to give a quantitative description of the present model. Within this approach one labels each part of the wavefunction on every conducting wire with a different amplitude which designates its traveling direction. Here, we use the following notation (as can be seen in the left panel of figure 3): L_1 designates the right-going amplitude of the wavefunction on the left lead while L_2 is the left-going amplitude on the same lead. Similarly, R_1 and R_2 stand for the right-and left-going wave amplitudes on the right lead, respectively. For the upper arm of the ring U_1 and U_2 represent the clockwise and counterclockwise traveling amplitudes, respectively, whereas D_2 and D_1 are the clockwise and counterclockwise traveling amplitudes on the lower arm.

Each junction is also assigned with appropriate scattering amplitudes. In what follows we assume that the junctions are identical and are characterized by scattering amplitudes as shown in the right panel of figure 3. a is the probability amplitude for an electron approaching the junction from one of the arms of the ring to be reflected back into the same arm, b is the probability amplitude to be transmitted from one arm of the ring to the other upon scattering at the junction and c is the probability amplitude for an electron approaching the junction from the lead to be reflected back into the lead. $\sqrt{\epsilon}$ is the probability amplitude to be transmitted to (or out of) either arms of the ring.

For each junction it is now possible to formulate a scattering matrix equation relating the outgoing wave amplitudes to the incoming wave amplitudes. For the left junction one gets

$$\begin{pmatrix} L_2 \\ U_1 \\ D_1 \end{pmatrix} = \begin{pmatrix} c & \sqrt{\epsilon} & \sqrt{\epsilon} \\ \sqrt{\epsilon} & a & b \\ \sqrt{\epsilon} & b & a \end{pmatrix} \begin{pmatrix} L_1 \\ U_2 e^{i\Phi_1} \\ D_2 e^{i\Phi_2} \end{pmatrix}. \tag{7}$$

Here $\Phi_1 = \Phi_k - \Phi_m$ is the phase accumulated by an electron traveling from the right junction to the left junction through the upper arm of the ring, and $\Phi_2 = \Phi_k + \Phi_m$ is the corresponding phase accumulated along the lower arm of the ring. Φ_k and $\Phi_m \equiv \Phi_m^u$ are defined in equations (3) and (4), respectively. An analogous equation can be written down for the right junction:

$$\begin{pmatrix} R_1 \\ U_2 \\ D_2 \end{pmatrix} = \begin{pmatrix} c & \sqrt{\epsilon} & \sqrt{\epsilon} \\ \sqrt{\epsilon} & a & b \\ \sqrt{\epsilon} & b & a \end{pmatrix} \begin{pmatrix} R_2 \\ U_1 e^{i\Phi_2} \\ D_1 e^{i\Phi_1} \end{pmatrix}. \tag{8}$$

In order to ensure current conservation during each scattering event at the junctions one has to enforce the scattering matrix to be unitary. This condition produces the following relations between the junction scattering amplitudes: $a = \frac{1}{2}(1 - c)$, $b = -\frac{1}{2}(1 + c)$ and $c = \sqrt{1 - 2\epsilon}$. It can be seen that the entire effect of the elastic scattering occurring at the junctions can be represented by a single parameter ϵ—the junction transmittance probability.

Solving these equations and setting the right incoming wave amplitude R_2 equal to zero, one gets a relation between the outgoing wave amplitude R_1 and the incoming wave amplitude L_1. Using this relation it is possible to calculate the transmittance probability through the ring which is given by [127, 111, 115]

$$T = \left|\frac{R_1}{L_1}\right|^2 = \frac{A[1 + \cos(2\phi_m)]}{1 + P\cos(2\phi_m) + Q\cos^2(2\phi_m)}, \tag{9}$$

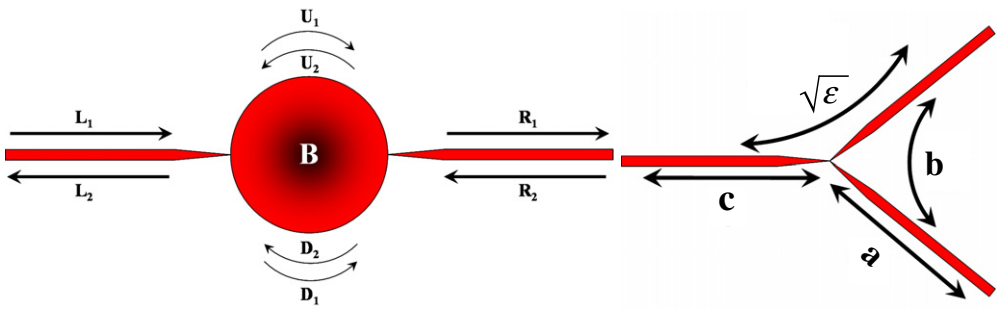

Figure 3. An illustration of the amplitudes of the different parts of the wavefunction (left panel) and the junction scattering amplitudes (right panel) in the 1D continuum model.

where the coefficients are functions of the spatial phase and the junction transmittance probability, and are given by [111]

$$A = \frac{16\epsilon^2[1-\cos(2\Phi_k)]}{R}$$
$$P = \frac{2(c-1)^2(c+1)^2 - 4(c^2+1)(c+1)^2\cos(2\Phi_k)}{R} \qquad (10)$$
$$Q = \frac{(c+1)^4}{R}$$
$$R = (c-1)^4 + 4c^4 + 4 - 4(c^2+1)(c-1)^2\cos(2\Phi_k) + 8c^2\cos(4\Phi_k).$$

The numerator of equation (9) resembles the result obtained for the interference of two distinct electron pathways (given by equation (6)). The correction for the case where the electrons are not absorbed at the detector is given by the denominator expression. An alternative approach to obtain the result given by equation (9) is based on a summation of all the paths of the electron entering the ring and completing $n + \frac{1}{2}$ loops before exiting, where n is the winding number. For $n = 0$ one recovers the simplified result of equation (6). The contribution of all higher-order terms ($n > 0$) is given by the denominator of equation (9).

From equations (9) and (10) it can be seen that two important independent parameters control the shape of the magneto-transmittance spectrum: the junction transmittance probability ϵ and the conducting electron wavenumber k appearing in the spatial phase $\Phi_k = \pi Rk$. In figure 4 we present the transmittance probability (T) through the ring as a function of the normalized magnetic flux threading it, for a given value of the spatial phase and several junction transmittance probabilities.

It can be seen that, for high values of the junction transmittance probability, the magneto-transmittance behavior is similar to that predicted by equation (6), i.e. a cosine function. As ϵ is reduced from its maximal value of $\frac{1}{2}$ the width of the transmittance peaks is narrowed. At large values of ϵ the lifetime of the electron on the ring is short and therefore the energy levels characterizing the ring are significantly broadened. Short lifetime also means that the electron traveling through the ring completes only very few cycles around it. In a path integral language, this implies that the interference pattern is governed by paths with low winding numbers. The application of a magnetic field will change the position of these energy levels: however, they will stay in partial resonance with the energy of the incoming electrons for a wide range of magnetic fields. Mathematically, the transmission through the ring when the electron exits the ring after it passes only along one of the arms can be reduced to the case where the detector is placed at the exit channel, and thus one would expect a cosine function describing the transmission as a function of magnetic field. When reducing the coupling (low values of ϵ) the doubly degenerate energy levels of the ring sharpen. If one assumes that at zero magnetic flux two such energy levels are in resonance with the incoming electrons, then upon applying a finite magnetic field the degeneracy is removed such that one level has its energy raised and the other lowered. This splitting

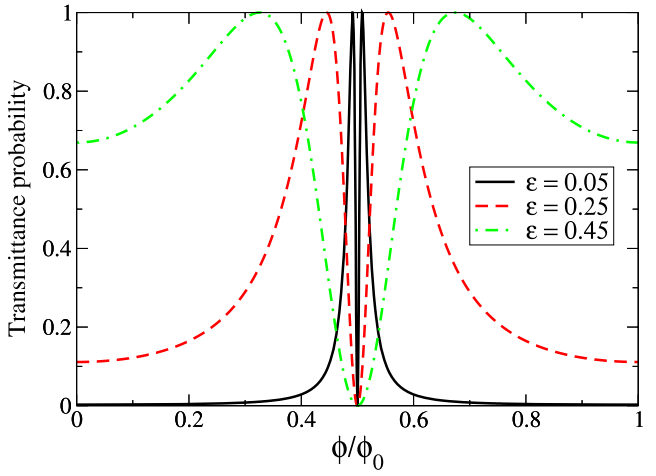

Figure 4. AB transmittance probability, calculated using equations (9) and (10), as a function of the magnetic flux for different junction transmittance probabilities and $kR = \frac{1}{2}$. For high values of ϵ (dashed–dotted line) the transmittance probability is similar to that predicted by equation (6). As ϵ is decreased the transmittance peaks narrow (dashed line). For very small values of ϵ the peaks become extremely narrow (solid line).

causes both sharp energy levels to shift out of resonance and thus reduces the transmittance probability through the ring dramatically. This, however, is not the case shown in figure 4, where the narrow transmittance peaks are located around the center of the AB period. Therefore, one needs to find a way to shift the transmittance resonances towards the low magnetic field region.

To gain such control we realize that the situation described above for the low coupling regime is, in fact, resonant tunneling occurring through the slightly broadened (due to the coupling to the leads) energy levels of a particle on a ring. Here, the free particle time-independent scattering wavefunction on the wires, $\psi_k(z) = e^{ikz}$, has the same form of the wavefunction of a particle on a ring $\psi_m(\theta) = e^{im\theta}$ where $m = 0, \pm1, \pm2, \ldots$. Upon mounting the ring, the electron's wavenumber, k_m, is quantized according to the following relation: $Rk_m = m$. The value of m for which resonant tunneling takes place is determined by the condition that the kinetic energy of the free electron on the wire equals a sharp energy eigenvalue of the ring [117, 128]:

$$\frac{\hbar^2k^2}{2m^\star} = \frac{\hbar^2(m-\frac{\phi}{\phi_0})^2}{2m^\star R^2}. \qquad (11)$$

In order to achieve resonance one has to require that $k = (m - \frac{\phi}{\phi_0})/R$. A slight change in the magnetic flux disrupts this resonance condition and reduces the transmittance considerably. For different values of the wavenumber on the leads the resonance condition in equation (11) will be obtained at different values of the magnetic flux.

This effect is depicted in figure 5 where the transmittance probability is plotted against the normalized magnetic flux threading the ring, for a given value of ϵ and several spatial phase factors. Changing the spatial phase results in a shift of the location of the transmittance peaks along the AB period.

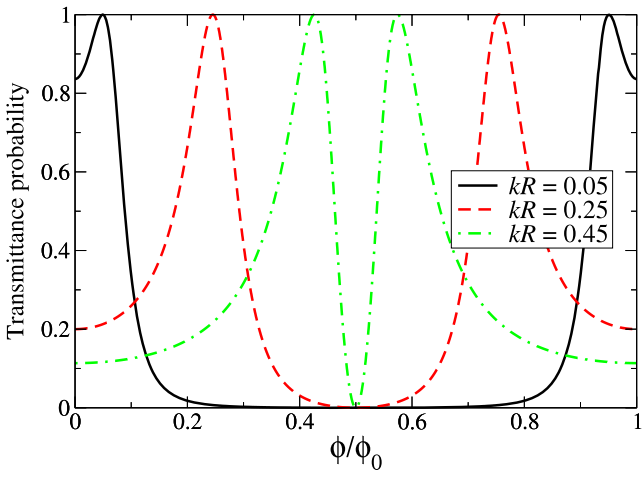

Figure 5. AB transmittance probability as a function of the magnetic flux for different spatial phases and $\epsilon = 0.25$. By changing the value of kR from $\sim n$ (dashed–dotted line) to $\sim n + \frac{1}{2}$ (solid line), where n is an integer, it is possible to shift the transmittance peaks from the center of the AB period to its edges.

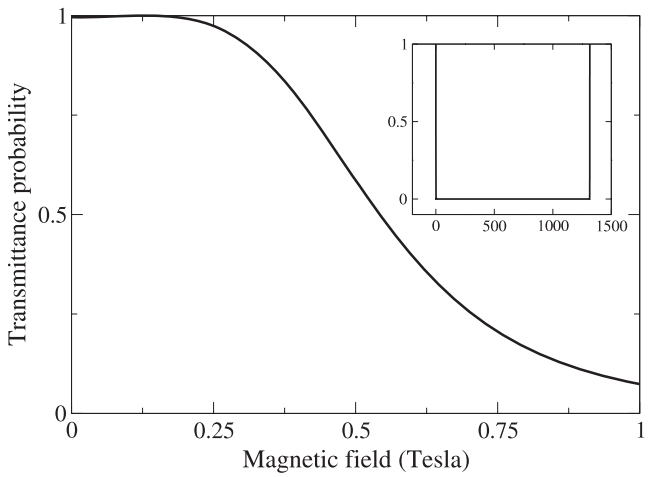

Figure 6. Low field magnetoresistance switching of a 1 nm ring weakly coupled to two conducting wires as calculated using the continuum model. The parameters chosen in this calculation are: $\epsilon = 0.005$ and $kR \approx 1$. Inset showing the full AB period of $\approx$1300 T.

This is analogous to the change in the position of the intensity peaks of the interference pattern observed in the optical double-slit experiment when varying the wavelength of the photons. For kR values of $\sim 0, 1, 2, \ldots$, the peaks are located near the center of the AB period, while for values of $\sim \frac{1}{2}, 1\frac{1}{2}, 2\frac{1}{2}, \ldots$ the peaks are shifted toward the period's lower and higher edges. In a realistic system such control can be achieved by the application of an electric gate field that serves to accelerate (or decelerate) the electron as it mounts the ring. The gate potential, V_g, thus modifies the resonance condition of equation (11) to

$$\frac{\hbar^2 k^2}{2m^\star} = \frac{\hbar^2 (m - \frac{\phi}{\phi_0})^2}{2m^\star R^2} + V_g. \tag{12}$$

Equation (12) implies that a change in the gate potential influences the magnetic flux at which resonance is attained. Therefore, the transmittance resonance's position along the AB period can be varied as shown in figure 5.

Considering the original goal of measuring a significant magnetoresistance effect in nanometer scale AB interferometers, it is clearly evident that, even though the full AB period is out of experimental reach, a delicate combination of an appropriate wavenumber of the conducting electrons and weak leads–ring coupling (so-called 'bad contact') enables us to shift the transmittance peak toward the low magnetic fields regime while at the same time dramatically increasing the sensitivity to the external magnetic field. The combined effect is discussed in figure 6, where magnetic switching for a 1 nm radius ring is obtained at a magnetic field of $\sim$1 T while the full AB period (see the inset of the figure) is achieved at magnetic fields orders of magnitude larger.

This result resembles the change in the interference intensity measured by the optical Mach–Zehnder interferometer [129, 130] upon altering the phase of the photons on one of the interferometric paths. The plausibility of applying these principles to realistic molecular systems is the subject of section 4. But first, an important question, which considers the uniqueness of using magnetic fields, has to be answered.

3.2. Three-terminal devices

A legitimate question that may be raised at this point is: why use magnetic fields to switch the conductance? Switching devices based on other external perturbations, such as field effect transistors (FETs), already exist and operate even at the molecular scale [51, 131, 52, 132, 55, 34, 59, 133, 60–68].

One simple answer is that magnetic fields can provide an additional control and perhaps for certain cases will enable control at small length scales where electrical fields are extremely hard to manipulate. However, as will become clear below, there are two additional motivations to employ magnetic fields as gates. One will be discussed shortly and the other involves inelastic effects which are described at the end of this review.

Consider an extension of the two-terminal continuum model described in section 3.1 to the case of three terminals. In a mesoscopic system or in the absence of magnetic fields, such devices have been considered by several groups (see [134–144]). An illustration of the three-terminal set-up is given in figure 7. The scattering matrix approach may be used in a similar manner to that described for the two-terminal set-up. An illustration of the three-terminal set-up parameters designation is given in figure 8. We denote (panel (a)) by α, β and $\gamma = 2\pi - \alpha - \beta$ the angles between the three conducting leads. Similar to the two-terminal model, we label the wave amplitudes on each ballistic conductor of the system as shown in panel (b) of figure 8.

The scattering amplitudes characterizing the junctions are given in figure 3 and obey the scattering matrix unitary condition: $c = \sqrt{1 - 2\epsilon}$, $a = \frac{1}{2}(1 - c)$ and $b = -\frac{1}{2}(1 + c)$. For simplicity, in what follows we assume that all the junctions

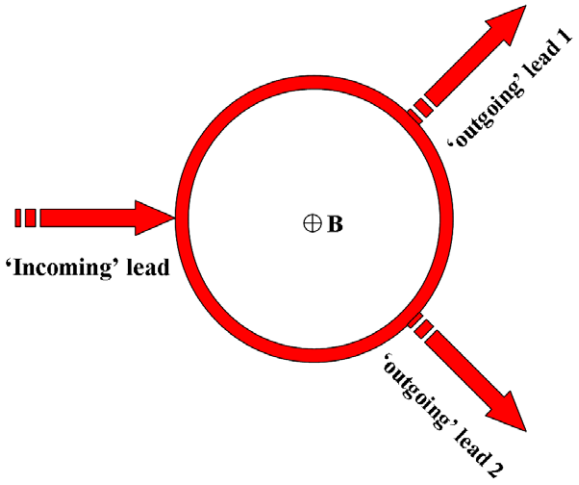

Figure 7. An illustration of a 1D coherent transport continuum model of a three-terminal AB interferometer.

are identical. This assumption can be easily corrected to the case of non-identical junctions.

Using these notations it is again possible to write scattering matrix relations between the incoming and outgoing wave amplitudes at each junction:

$$\begin{pmatrix} L_2 \\ U_1 \\ D_1 \end{pmatrix} = \begin{pmatrix} c & \sqrt{\epsilon} & \sqrt{\epsilon} \\ \sqrt{\epsilon} & a & b \\ \sqrt{\epsilon} & b & a \end{pmatrix} \begin{pmatrix} L_1 \\ U_2 e^{i\Phi_1^{\alpha}} \\ D_2 e^{i\Phi_2^{\beta}} \end{pmatrix}$$
$$\begin{pmatrix} R_1 \\ M_1 \\ U_2 \end{pmatrix} = \begin{pmatrix} c & \sqrt{\epsilon} & \sqrt{\epsilon} \\ \sqrt{\epsilon} & a & b \\ \sqrt{\epsilon} & b & a \end{pmatrix} \begin{pmatrix} R_2 \\ M_2 e^{i\Phi_1^{\gamma}} \\ U_1 e^{i\Phi_2^{\alpha}} \end{pmatrix} \qquad (13)$$
$$\begin{pmatrix} I_1 \\ D_2 \\ M_2 \end{pmatrix} = \begin{pmatrix} c & \sqrt{\epsilon} & \sqrt{\epsilon} \\ \sqrt{\epsilon} & a & b \\ \sqrt{\epsilon} & b & a \end{pmatrix} \begin{pmatrix} I_2 \\ D_1 e^{i\Phi_1^{\beta}} \\ M_1 e^{i\Phi_2^{\gamma}} \end{pmatrix}.$$

Here $\Phi_1^{\Delta=\alpha,\beta,\gamma} = \Delta Rk - \Delta\frac{\phi}{\phi_0}$ and $\Phi_2^{\Delta=\alpha,\beta,\gamma} = \Delta Rk + \Delta\frac{\phi}{\phi_0}$. Eliminating the equations for the wave amplitudes on the ring ($U_{1,2}$, $D_{1,2}$, $M_{1,2}$), similar to the two-terminal continuum model treatment, and plugging the solution into the equations for the outgoing amplitudes, I_1 and R_1, one finds a relation between the incoming amplitude on the left lead L_1 and both outgoing amplitudes. The probability to transmit through the upper (lower) outgoing lead is given by $T^u = |\frac{R_1}{L_1}|^2$ ($T^l = |\frac{I_1}{L_1}|^2$). The exact expressions for these transmittance probabilities, even when setting the incoming wave amplitudes R_2 and I_2 to zero, are somewhat tedious to obtain [145]. Thus, we provide the final results for completeness.

The denominator of the transmittance probability for both output channels is given by the following expression:

$$\begin{aligned} T_{\text{denominator}} &= \tfrac{1}{16}(c^2+1)(19-12c+2c^2-12c^3+19c^4) \\ &+ 32c^3\cos(4\pi kr) + 2(c-1)^4 c\{\cos[4\pi kr(1-2\alpha)] \\ &+ \cos[4\pi kr(1-2\beta)] + \cos[4\pi kr(1-2\gamma)]\} \\ &- 8(c-1)^2 c(c^2+1)\{\cos[4\pi kr(\alpha-1)] \\ &+ \cos[4\pi kr(\beta-1)] + \cos[4\pi kr(\gamma-1)]\} \\ &- 4(c-1)^2(2-c+2c^2-c^3+2c^4)[\cos(4\pi kr\alpha) \\ &+ \cos(4\pi kr\beta) + \cos(4\pi kr\gamma)] \\ &+ 2(c-1)^4(c^2+1)\{\cos[4\pi kr(\alpha-\beta)] \\ &+ \cos[4\pi kr(\alpha-\gamma)] + \cos[4\pi kr(\beta-\gamma)]\} \\ &- 0.125(c+1)^4 \times \{-4[1+c(c-1)]\cos(2\pi kr) \\ &+ (c-1)^2[\cos[2\pi kr(1-2\alpha)] + \cos[2\pi kr(1-2\beta)] \\ &+ \cos[2\pi kr(1-2\gamma)]]\}\cos\left(2\pi\frac{\phi}{\phi_0}\right) \\ &+ \frac{1}{16}(c+1)^6\cos^2\left(2\pi\frac{\phi}{\phi_0}\right). \end{aligned} \qquad (14)$$

The numerator of the transmittance probability through the upper output channel is given by

$$\begin{aligned} T^u_{\text{numerator}} &= -\tfrac{1}{2}\epsilon^2\Big\{-4(1+c^2) + 2(c-1)^2\cos(4\pi kr\alpha) \\ &+ (c+1)^2\cos(4\pi kr\beta) + 2(c-1)^2\cos(4\pi kr\gamma) \\ &+ 4c\cos[4\pi kr(\alpha+\gamma)] - (c-1)^2\cos[4\pi kr(\alpha-\gamma)] \\ &- 2c(c+1)\cos\left[2\pi\left(\frac{\phi}{\phi_0}-kr\right)\right] \\ &- 2(c+1)\cos\left[2\pi\left(\frac{\phi}{\phi_0}+kr\right)\right] \end{aligned}$$

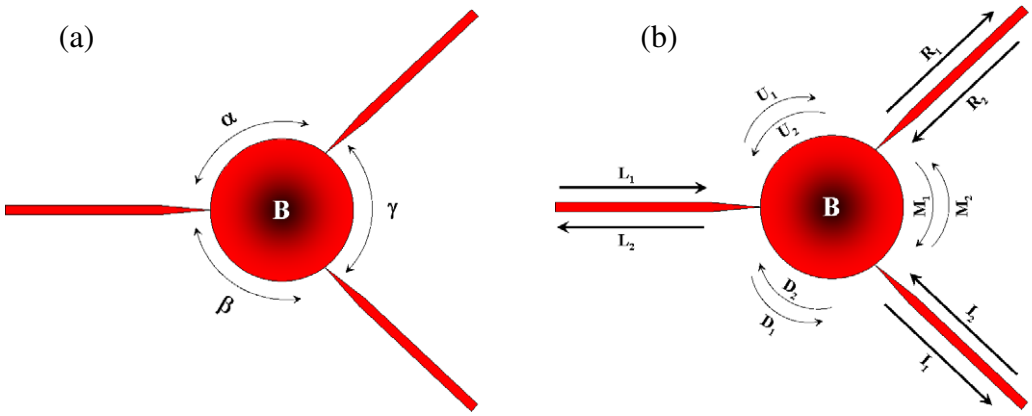

Figure 8. Parameter designations in the three-terminal continuum model. Panel (a): the angular separations between the three terminals. Panel (b): the amplitudes of different parts of the wavefunction.

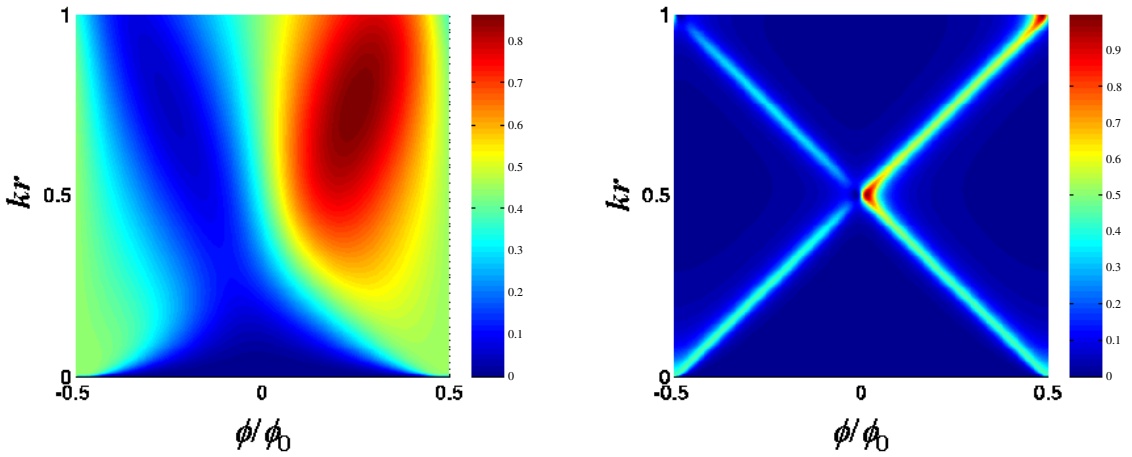

Figure 9. The transmittance of a three-terminal device as a function of the magnetic flux and the wavenumber of the conducting electron as calculated using the continuum model. Left panel: high coupling ($\epsilon = 0.495$), right panel: low coupling ($\epsilon = 0.095$). Color code: deep blue—no transmittance ($T = 0$), deep red—full transmittance ($T = 1$).

$$
\begin{aligned}
&- (c^2-1)\cos\left[2\pi\left(\frac{\phi}{\phi_0}+(1-2\alpha)kr\right)\right]\\
&+ (c^2-1)\cos\left[2\pi\left(\frac{\phi}{\phi_0}-(1-2\alpha)kr\right)\right]\\
&+ 2(c+1)\cos\left[2\pi\left(\frac{\phi}{\phi_0}+(1-2\beta)kr\right)\right]\\
&+ 2c(c+1)\cos\left[2\pi\left(\frac{\phi}{\phi_0}-(1-2\beta)kr\right)\right]\\
&- (c^2-1)\cos\left[2\pi\left(\frac{\phi}{\phi_0}+(1-2\gamma)kr\right)\right]\\
&+ (c^2-1)\cos\left[2\pi\left(\frac{\phi}{\phi_0}-(1-2\gamma)kr\right)\right]\Bigg\}. \qquad (15)
\end{aligned}
$$

The numerator of the transmittance probability through the lower output channel is given by

$$
\begin{aligned}
T^{l}_{\text{numerator}} = -\tfrac{1}{2}\epsilon^2\Bigg\{&-4(1+c^2)+(c+1)^2\cos(4\pi kr\alpha)\\
&+2(c-1)^2\cos(4\pi kr\beta)+2(c-1)^2\cos(4\pi kr\gamma)\\
&+4c\cos[4\pi kr(\beta+\gamma)]-(c-1)^2\cos[4\pi kr(\beta-\gamma)]\\
&-2c(c+1)\cos\left[2\pi\left(\frac{\phi}{\phi_0}+kr\right)\right]\\
&-2(c+1)\cos\left[2\pi\left(\frac{\phi}{\phi_0}-kr\right)\right]\\
&+2c(c+1)\cos\left[2\pi\left(\frac{\phi}{\phi_0}+(1-2\alpha)kr\right)\right]\\
&+2(c+1)\cos\left[2\pi\left(\frac{\phi}{\phi_0}-(1-2\alpha)kr\right)\right]\\
&+(c^2-1)\cos\left[2\pi\left(\frac{\phi}{\phi_0}+(1-2\beta)kr\right)\right]\\
&-(c^2-1)\cos\left[2\pi\left(\frac{\phi}{\phi_0}-(1-2\beta)kr\right)\right]\\
&+(c^2-1)\cos\left[2\pi\left(\frac{\phi}{\phi_0}+(1-2\gamma)kr\right)\right]\\
&-(c^2-1)\cos\left[2\pi\left(\frac{\phi}{\phi_0}-(1-2\gamma)kr\right)\right]\Bigg\}. \qquad (16)
\end{aligned}
$$

The back-scattering probability is the complementary part of the sum of the transmittance probability through both the upper and lower leads.

The resulting transmittance probability through one of the outgoing leads, for the symmetric case where $\alpha = \beta = \gamma = \frac{2\pi}{3}$, is presented in figure 9 as a function of the magnetic flux threading the ring and the wavenumber of the conducting electron. In the high coupling limit (left panel of figure 9) the system is characterized by a wide range of high transmittance which can be shifted along the AB period by changing the electron's wavenumber. Magnetic switching of the transmittance at a given wavenumber value for this coupling regime requires high magnetic fields, since the transmittance peaks are quite broad.

As the coupling is decreased from its maximal value of $\epsilon = \frac{1}{2}$ to very low values (right panel of figure 9), a resonant tunneling junction is formed and the transmittance probability becomes very sensitive to the magnetic flux. Similar to the two-terminal case, this is translated into sharper peaks that develop in the magneto-transmittance curve. For the parameters shown in the right panel of figure 9 there is negligible transmittance for all values of k at zero magnetic field. Note that the position of the first maximum in the transmittance depends linearly on the value of ϕ and k. Fine tuning the wavenumber to a value that satisfies $kR = \frac{1}{2}$ results in the appearance of the sharp transmittance peak at finite, relatively low, magnetic flux and thus allows the switching of the device at feasible magnetic fields.

A careful examination of the transmittance probability spectrum for $kR = \frac{1}{2}$ at the low magnetic flux regime reveals that the appearance of the transmittance peak is sensitive to the polarity of the magnetic flux. While at a positive magnetic flux a pronounced peak is observed, at the negative magnetic

flux counterpart this peak is absent. This magnetic rectification phenomena is, allegedly, in contrast to the Onsager symmetry relation [146–148, 127], obeyed in the two-terminal case which states that $g(\phi) = g(-\phi)$ where g is the conductance.

This contradiction is resolved by considering the transmittance probability through the other output channel, which can be obtained by applying a reflection transformation with respect to a plain passing through the incoming lead and perpendicular to the cross section of the ring. The Hamiltonian of the system is invariant to such a transformation only if accompanied by a reversal of the direction of the magnetic field. It follows that the transmittance probability through one outgoing lead is the mirror image of the transmittance through the other. Thus, one finds that for the second output channel (not shown) the peak is observed at a negative magnetic flux rather than at a positive one. Onsager's condition is, therefore, regained for the sum of the transmittance probabilities through both output channels.

The above analysis implies that at zero magnetic field both output channels are closed and the electron is totally reflected. The application of a relatively small positive magnetic field opens only one output channel and forces the electrons to transverse the ring through this channel alone. Reversing the polarity of the magnetic field causes the output channels to interchange roles and forces the electrons to pass through the ring via the other lead.

To summarize this section, magnetic fields offer unique controllability over the conductance of nanometer-scale interferometers. For example, their polarity can be used to selectively switch different conducting channels. While *non-uniform* scalar potentials have been used in *mesoscopic* physics to obtain a similar effect [149], such control cannot be obtained via the application of uniform scalar potentials, which are commonly used to control molecular-scale devices. This is due to the fact that such scalar potentials lack the symmetry breaking nature of magnetic vector potentials.

4. Atomistic calculations

The models presented in section 3 are based on a simplified description where the AB interferometers were modeled within a continuum approach. In order to capture the more complex nature of the electronic structure of realistic nanoscale AB interferometers we consider a model which was developed for the calculation of magnetoconductance through molecular set-ups [112]. The approach is based on an extension of a tight binding extended Hückel approach which incorporates the influence of external magnetic fields. This approach is combined with a nonequilibrium Green's function (NEGF) [150, 151] formalism to calculate the conduction [152, 119, 153–155]. In the case of pure elastic scattering, this reduces to the Landauer formalism, which relates the conductance to the transmittance probability through the system [153]. The resulting magnetoconductance spectrum can then be studied for different molecular set-ups and conditions, as described below.

4.1. Conductance

We are interested in calculating the conductance through a molecular device coupled to two macroscopic conducting leads in the presence of an external magnetic field. For completeness, we provide the details of the approach adopted for the present study. For more details on the theory of molecular conduction, see [119, 5, 8, 12, 156].

The starting point is the current formula obtained within the NEGF framework [153]:

$$I_{\mathrm{L(R)}} = \frac{2e}{\hbar}\int \frac{\mathrm{d}E}{2\pi}\mathrm{Tr}\left[\Sigma^{<}_{\mathrm{L(R)}}(E)G^{>}_{\mathrm{d}}(E) - \Sigma^{>}_{\mathrm{L(R)}}G^{<}_{\mathrm{d}}(E)\right]. \tag{17}$$

Here $I_{\mathrm{L(R)}}$ is the net current measured at the left (right) molecule–lead junction, $G^{<}_{\mathrm{d}}(E)$ and $G^{>}_{\mathrm{d}}(E)$ are the lesser and greater device Green's functions, respectively, and $\Sigma^{<}_{\mathrm{L(R)}}$ and $\Sigma^{>}_{\mathrm{L(R)}}$ are the left (right) lesser and greater self-energy terms, respectively. The first term in the trace in equation (17) can be identified with the rate of in-scattering of electrons into the device from the left (right) lead. Similarly, the second term represents the out-scattering rate of electrons into the left (right) lead. The difference between these two terms gives the net, energy-dependent, flow rate of electrons through the device. When integrated over the energy and multiplied by twice (to account for spin states) the electron's charge, this results in the net current flowing through the left (right) junction. It can be shown [157] that $I_{\mathrm{L}} = -I_{\mathrm{R}}$ in analogy to Kirchhoff's law, and therefore equation (17) represents the full current through the device.

The lesser and greater GFs appearing in equation (17) are related to the retarded ($G^{\mathrm{r}}(E)$) and advanced ($G^{\mathrm{a}}(E)$) GFs, which will be discussed later, through the Keldysh equation [150]:

$$\begin{aligned} G^{<}_{\mathrm{d}}(E) &= G^{\mathrm{r}}_{\mathrm{d}}(E)\Sigma^{<}(E)G^{\mathrm{a}}_{\mathrm{d}}(E) \\ G^{>}_{\mathrm{d}}(E) &= G^{\mathrm{r}}_{\mathrm{d}}(E)\Sigma^{>}(E)G^{\mathrm{a}}_{\mathrm{d}}(E), \end{aligned} \tag{18}$$

We now limit our discussion to the pure elastic case within a single-electron picture, where, as pointed out above, the NEGF approach reduces to the Landauer formalism [153]. We retain the description within the NEGF to provide a complete description needed below when inelastic effects will be considered. In the pure elastic scattering case one assumes that the lesser (greater) self-energies have contributions arising from the coupling to the left and right leads only:

$$\begin{aligned} \Sigma^{<} &= \Sigma^{<}_{\mathrm{L}} + \Sigma^{<}_{\mathrm{R}} \\ \Sigma^{>} &= \Sigma^{>}_{\mathrm{L}} + \Sigma^{>}_{\mathrm{R}}. \end{aligned} \tag{19}$$

Furthermore, the lesser and greater self-energy terms in equations (17) and (19) are related to the retarded ($\Sigma^{\mathrm{r}}_{\mathrm{L(R)}}(E)$) and advanced ($\Sigma^{\mathrm{a}}_{\mathrm{L(R)}}(E)$) self-energies, which will also be discussed later, in the following manner:

$$\begin{aligned} \Sigma^{<}_{\mathrm{L(R)}}(E) &= -f_{\mathrm{L(R)}}(E,\mu_{\mathrm{L(R)}})\left[\Sigma^{\mathrm{r}}_{\mathrm{L(R)}}(E) - \Sigma^{\mathrm{a}}_{\mathrm{L(R)}}(E)\right] \\ \Sigma^{>}_{\mathrm{L(R)}}(E) &= \left[1 - f_{\mathrm{L(R)}}(E,\mu_{\mathrm{L(R)}})\right]\left[\Sigma^{\mathrm{r}}_{\mathrm{L(R)}}(E) - \Sigma^{\mathrm{a}}_{\mathrm{L(R)}}(E)\right], \end{aligned} \tag{20}$$

where $f_{L(R)}(E,\mu_{L(R)}) = [1+e^{\beta(E-\mu_{L(R)})}]^{-1}$ is the Fermi–Dirac occupation distribution in the left (right) lead, $\mu_{L(R)}$ is the electrochemical potential of the left (right) lead and $\beta = \frac{1}{k_B T}$, where k_B is Boltzmann's constant and T is the temperature. Upon plugging equations (18) and (20) into (17), one obtains the following result for the current:

$$I = \frac{2e}{\hbar}\int \frac{dE}{2\pi}\left[f_L(E,\mu_L) - f_R(E,\mu_R)\right] \times \mathrm{Tr}\left[\Gamma_L(E)G_d^r(E)\Gamma_R(E)G_d^a(E)\right], \quad (21)$$

where the level broadening matrix $\Gamma_{L(R)}$ is given by

$$\Gamma_{L(R)}(E) \equiv i\left[\Sigma_{L(R)}^r(E) - \Sigma_{L(R)}^a(E)\right]. \quad (22)$$

It is now possible to identify $T(E) = \mathrm{Tr}[\Gamma_L(E)G_d^r(E)\Gamma_R(E)G_d^a(E)]$ as the electron transmission probability through the molecule and the difference in the Fermi–Dirac distribution functions as the net, energy-dependent, density of current carrying particles from the left (right) lead to the right (left) lead, due to the difference in their electrochemical potentials [120]. The current is obtained by integration over the energy.

For calculating the conductance (g) one can define the differential conductance as the derivative of the current with respect to the applied bias voltage (V_b):

$$g = \frac{\partial I}{\partial V_b} = \frac{2e}{\hbar}\frac{\partial}{\partial V_b}\int \frac{dE}{2\pi}\left[f_L(E,\mu_L) - f_R(E,\mu_R)\right] \times \mathrm{Tr}\left[\Gamma_L(E)G_d^r(E)\Gamma_R(E)G_d^a(E)\right]. \quad (23)$$

If one assumes that the bias voltage applied does not alter considerably the energetic structure of the device, the only contribution of the bias in equation (21) appears in the Fermi–Dirac distribution functions. Therefore, it is possible to directly conduct the differentiation in equation (23) to get the following relation:

$$g = \frac{\partial I}{\partial V_b} = \frac{2e}{\hbar}\int \frac{dE}{2\pi}\frac{\partial\left[f_L(E,\mu_L) - f_R(E,\mu_R)\right]}{\partial V_b} \times \mathrm{Tr}\left[\Gamma_L(E)G_d^r(E)\Gamma_R(E)G_d^a(E)\right]. \quad (24)$$

It should be noted that for finite bias voltages the above equation is valid only in the so-called wide band limit (WBL) or in the single-electron limit [257].

If one further assumes that the bias potential drops sharply and equally at both junctions [158], the electrochemical potentials are given by $\mu_{L(R)} = E_f^{L(R)} + (-)\frac{1}{2}eV_b$, where $E_f^{L(R)}$ is the Fermi energy of the left (right) lead. Thus, the derivative with respect to the bias voltage appearing in equation (24) is given by

$$\frac{\partial\left[f_L(E,\mu_L) - f_R(E,\mu_R)\right]}{\partial V_b} = \frac{e\beta}{2}\left\{\frac{e^{-\beta|E-\mu_L|}}{\left[1+e^{-\beta|E-\mu_L|}\right]^2} + \frac{e^{-\beta|E-\mu_R|}}{\left[1+e^{-\beta|E-\mu_R|}\right]^2}\right\}. \quad (25)$$

If both Fermi energies of the leads are aligned with the Fermi energy of the device, and the electrochemical potential difference arises from the bias voltage alone, then at the limit of zero temperature and zero bias conductance the expression appearing in equation (25) approaches a sharp δ function located at the Fermi energy of the molecule and equation (23), in turn, reduces to the well established Landauer formula [119, 159], which directly relates the conductance to the transmittance probability of the current carrying entity through the relevant device:

$$g = g_0 T, \quad (26)$$

where $g_0 = \frac{2e^2}{h}$ is the conductance quantum.

Considering the full expression given by equation (24) it can be seen that, for the calculation of the conductance, or more specifically of the transmittance probability, it is necessary to obtain the retarded and advanced GFs of the device and the retarded and advanced self-energies of the leads. Obtaining these is the subject of the next section.

4.2. Retarded and advanced Green's functions and self-energies

Following the lines of NEGF theory [153], the GF associated with a Hamiltonian $\hat{H}$ evaluated in a non-orthogonal basis set must satisfy the following relation in energy space [160]:

$$(E\hat{S} - \hat{H})\hat{G}(E) = \hat{I}, \quad (27)$$

where E is the energy, $\hat{S}$ is the overlap matrix, $\hat{G}(E)$ is the GF and $\hat{I}$ a unit matrix of the appropriate dimensions.

As suggested above, in molecular conductance calculations it is customary to divide the system into the 'device', which is the conducting molecule[5], and the 'leads', which are the macroscopic conducting contacts through which electrons are injected into and taken out of the 'device'. In a two-terminal set-up this is translated into the following sub-matrices division of equation (27) [160, 161]:

$$\begin{pmatrix} \epsilon\hat{S}_L - \hat{H}_L & \epsilon\hat{S}_{Ld} - \hat{V}_{Ld} & 0 \\ \epsilon\hat{S}_{dL} - \hat{V}_{dL} & \epsilon\hat{S}_d - \hat{H}_d & \epsilon\hat{S}_{dR} - \hat{V}_{dR} \\ 0 & \epsilon\hat{S}_{Rd} - \hat{V}_{Rd} & \epsilon\hat{S}_R - \hat{H}_R \end{pmatrix} \times \begin{pmatrix} \hat{G}_L^r(\epsilon) & \hat{G}_{Ld}^r(\epsilon) & \hat{G}_{LR}^r(\epsilon) \\ \hat{G}_{dL}^r(\epsilon) & \hat{G}_d^r(\epsilon) & \hat{G}_{dR}^r(\epsilon) \\ \hat{G}_{RL}^r(\epsilon) & \hat{G}_{Rd}^r(\epsilon) & \hat{G}_R^r(\epsilon) \end{pmatrix} = \begin{pmatrix} \hat{I}_L & \hat{0} & \hat{0} \\ \hat{0} & \hat{I}_d & \hat{0} \\ \hat{0} & \hat{0} & \hat{I}_R \end{pmatrix}. \quad (28)$$

Here, $\hat{H}_{L(R)}$ and $\hat{H}_d$ are the left (right) semi-infinite lead and the device Hamiltonians, respectively, $\hat{S}_{L(R)}$ and $\hat{S}_d$ are the left (right) lead and the device overlap matrices, respectively, $\hat{V}_{L(R)d}$ are the coupling matrices between the left (right) lead and the device and $\hat{S}_{L(R)d}$ are the overlap matrices between the left (right) lead and the device. Since the Hamiltonian is Hermitian one finds that $\hat{V}_{dL(R)} = \hat{V}_{L(R)d}^\dagger$, and the same requirement applies for the overlap matrices $\hat{S}_{dL(R)} = \hat{S}_{L(R)d}^\dagger$ (see section 4.4). All the terms discussed above are calculated

[5] Usually one defines an 'extended molecule' which is the molecule itself accompanied with a limited portion of the leads which is influenced by the proximity to the molecule.

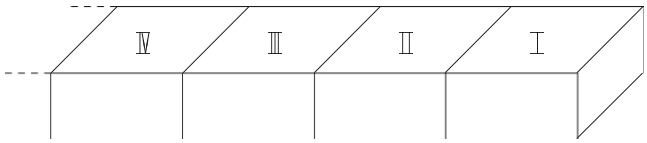

Figure 10. Division of the semi-infinite bulk lead into a set of nearest-neighbors interacting layers.

using a formalism which will be presented in section 4.4. A complex energy $\epsilon = \lim_{\eta\to 0}\{E + \mathrm{i}\eta\}$ has been introduced in order to shift the poles of the Green's function from the real axis and allow for the convergence of both an analytical and a numerical evaluation of the integrals over the GFs. This softens the sharp singularities of the GF into a smoother Lorentzian shape which in the limit of $\eta \to 0$ restores the δ function characteristics of the imaginary part.

Solving equation (28) for the middle column of the GF matrix results in the following expression for the retarded device GF (which appears in equation (24)) $\hat{G}^{\mathrm{r}}_{\mathrm{d}}(\epsilon)$, when coupled to the two leads:

$$\hat{G}^{\mathrm{r}}_{\mathrm{d}}(\epsilon) = \left[\left(g^{\mathrm{r}}_{\mathrm{d}}(\epsilon)\right)^{-1} - \hat{\Sigma}^{\mathrm{r}}_{\mathrm{L}}(\epsilon) - \hat{\Sigma}^{\mathrm{r}}_{\mathrm{R}}(\epsilon)\right]^{-1}, \tag{29}$$

where $\hat{g}^{\mathrm{r}}_{\mathrm{d}}(\epsilon) = [\epsilon\hat{S}_{\mathrm{d}} - \hat{H}_{\mathrm{d}}]^{-1}$ is the retarded GF of the bare device and $\hat{\Sigma}^{\mathrm{r}}_{\mathrm{L(R)}}(\epsilon)$ is the retarded self-energy of the left (right) lead given by

$$\hat{\Sigma}^{\mathrm{r}}_{\mathrm{L(R)}}(\epsilon) = \left(\epsilon\hat{S}_{\mathrm{dL(R)}} - \hat{H}_{\mathrm{dL(R)}}\right)\hat{g}^{\mathrm{r}}_{\mathrm{L(R)}}(\epsilon) \times \left(\epsilon\hat{S}_{\mathrm{L(R)d}} - \hat{H}_{\mathrm{L(R)d}}\right). \tag{30}$$

Here, $\hat{g}^{\mathrm{r}}_{\mathrm{L(R)}}(\epsilon) = [\epsilon\hat{S}_{\mathrm{L(R)}} - \hat{H}_{\mathrm{L(R)}}]^{-1}$ is the retarded GF of the bare left (right) lead. The advanced device GF is the Hermitian conjugate of its retarded counterpart $\hat{G}^{\mathrm{a}}_{\mathrm{d}}(\epsilon) = [\hat{G}^{\mathrm{r}}_{\mathrm{d}}(\epsilon)]^{\dagger}$.

The self-energy terms appearing in equations (29) and (30) represent the effect of the coupling to the leads on the GF of the device. The calculation of these terms requires the GF of the bare lead $\hat{g}^{\mathrm{r}}_{\mathrm{L(R)}}(\epsilon)$. This is not a simple task since the leads are macroscopic sources of electrons whose GFs are impossible to calculate directly. A way to overcome this obstacle is to represent the leads as periodic bulk structures of a semi-infinite nature. Using common solid state physics techniques the periodicity of the bulk can considerably reduce the dimensionality of the problem and thus enables the calculation of the electronic structure of the leads. For this, one can use an efficient iterative procedure developed by López Sancho *et al* [162–164]. Within this approach the semi-infinite bulk is divided into a set of identical principal layers, as shown in figure 10, in such a manner that only adjacent layers overlap and interact. Using equation (27) the resulting GF can be represented as the inverse of a nearest-neighbors block-tridiagonal matrix of the form

$$\begin{pmatrix} \hat{G}_{00}(\epsilon) & \hat{G}_{01}(\epsilon) & \hat{G}_{02}(\epsilon) & \hat{G}_{03}(\epsilon) & \cdots \\ \hat{G}_{10}(\epsilon) & \hat{G}_{11}(\epsilon) & \hat{G}_{12}(\epsilon) & \hat{G}_{13}(\epsilon) & \cdots \\ \hat{G}_{20}(\epsilon) & \hat{G}_{21}(\epsilon) & \hat{G}_{22}(\epsilon) & \hat{G}_{23}(\epsilon) & \cdots \\ \hat{G}_{30}(\epsilon) & \hat{G}_{31}(\epsilon) & \hat{G}_{32}(\epsilon) & \hat{G}_{33}(\epsilon) & \cdots \\ \vdots & \vdots & \vdots & \vdots & \ddots \end{pmatrix}$$

$$= \begin{pmatrix} \epsilon\hat{S}_{00} - \hat{H}_{00} & \epsilon\hat{S}_{01} - \hat{V}_{01} & 0 & 0 & \cdots \\ \epsilon\hat{S}_{10} - \hat{V}_{10} & \epsilon\hat{S}_{00} - \hat{H}_{00} & \epsilon\hat{S}_{01} - \hat{V}_{01} & 0 & \cdots \\ 0 & \epsilon\hat{S}_{10} - \hat{V}_{10} & \epsilon\hat{S}_{00} - \hat{H}_{00} & \epsilon\hat{S}_{01} - \hat{V}_{01} & \cdots \\ 0 & 0 & \epsilon\hat{S}_{10} - \hat{V}_{10} & \epsilon\hat{S}_{00} - \hat{H}_{00} & \cdots \\ \vdots & \vdots & \vdots & \vdots & \ddots \end{pmatrix}^{-1}. \tag{31}$$

Here, $\hat{S}_{\mathrm{I,I}} = \hat{S}_{\mathrm{II,II}} = \hat{S}_{\mathrm{III,III}} = \cdots \equiv \hat{S}_{00}$ is the overlap matrix of the principal layer with itself, $\hat{S}_{\mathrm{I,II}} = \hat{S}_{\mathrm{II,III}} = \hat{S}_{\mathrm{III,IV}} = \cdots \equiv \hat{S}_{01}$ is the overlap matrix between two adjacent layers and, as before, $\hat{S}_{10} = [\hat{S}_{01}]^{\dagger}$. $\hat{H}_{\mathrm{I,I}} = \hat{H}_{\mathrm{II,II}} = \hat{H}_{\mathrm{III,III}} = \cdots \equiv \hat{H}_{00}$ is the Hamiltonian matrix of the principal layer, $\hat{V}_{\mathrm{I,II}} = \hat{V}_{\mathrm{II,III}} = \hat{V}_{\mathrm{III,IV}} = \cdots \equiv \hat{V}_{01}$ is the coupling matrix between two adjacent layers and $\hat{V}_{10} = [\hat{V}_{01}]^{\dagger}$.

Equation (31) is a matrix representation of a set of equations for the semi-infinite bulk GF matrix elements $\hat{G}_{ij}(\epsilon)$ which can be solved iteratively to get a compact expression:

$$\hat{G}(\epsilon) = \left[(\epsilon\hat{S}_{00} - \hat{H}_{00}) + (\epsilon\hat{S}_{01} - \hat{H}_{01})T(\epsilon) + (\epsilon\hat{S}^{\dagger}_{01} - \hat{H}^{\dagger}_{01})\overline{T}(\epsilon)\right]^{-1}. \tag{32}$$

The transfer matrices T and $\overline{T}$ are given by converging series of the form

$$\begin{aligned} T(\epsilon) &= t_0 + \tilde{t}_0 t_1 + \tilde{t}_0\tilde{t}_1 t_2 + \cdots + \tilde{t}_0\tilde{t}_1\tilde{t}_2\cdots t_n \\ \overline{T}(\epsilon) &= \tilde{t}_0 + t_0\tilde{t}_1 + t_0 t_1\tilde{t}_2 + \cdots + t_0 t_1 t_2\cdots\tilde{t}_n, \end{aligned} \tag{33}$$

where t_i and $\tilde{t}_i$ are defined by the recursion relations:

$$\begin{aligned} t_i &= \left(I - t_{i-1}\tilde{t}_{i-1} - \tilde{t}_{i-1}t_{i-1}\right)^{-1} t^2_{i-1} \\ \tilde{t}_i &= \left(I - t_{i-1}\tilde{t}_{i-1} - \tilde{t}_{i-1}t_{i-1}\right)^{-1} \tilde{t}^2_{i-1}, \end{aligned} \tag{34}$$

with the following initial conditions:

$$\begin{aligned} t_0 &= \left(\epsilon\hat{S}_{00} - \hat{H}_{00}\right)^{-1} V^{\dagger}_{01} \\ \tilde{t}_0 &= \left(\epsilon\hat{S}_{00} - \hat{H}_{00}\right)^{-1} V_{01}. \end{aligned} \tag{35}$$

After calculating the semi-infinite bulk GF given in equation (32), the left and right lead self-energies can be determined using equation (30) and the $\hat{\Gamma}_{\mathrm{L(R)}}$ matrices appearing in the conductance expression (equation (24)) can be calculated using equation (22) with $\hat{\Sigma}^{\mathrm{a}}_{\mathrm{L(R)}}(\epsilon) = [\hat{\Sigma}^{\mathrm{r}}_{\mathrm{L(R)}}(\epsilon)]^{\dagger}$.

4.3. An alternative—absorbing imaginary potentials

A second methodology for the calculation of the transmittance probability involves the application of absorbing potentials [166, 167]. Within this approach the $\Gamma_{L(R)}$ matrix appearing in equation (24) is a negative imaginary potential placed deep within the left (right) lead. The purpose of this potential is to absorb an electron traveling in the lead away from the molecular device before it reaches the 'edge' of the lead. This ensures that the effect of reflections from the distant lead edge is suppressed to a desired accuracy and thus enables us to truncate the lead representation to a computable size.

In this review we show results that are based on a Gaussian approximation to the imaginary absorbing potentials of the form $V_{L(R)} = V_0 e^{-\frac{(z-z_0^{L(R)})^2}{2\sigma^2}}$. Here, V_0 is the potential height, σ the potential width and $z_0^{L(R)}$ its location along the left (right) lead, assuming that the leads are located along the Z axis. The generalization of the above expression to the case of an arbitrary lead direction is straightforward. The parameters of the potential are chosen such that electrons possessing a kinetic energy in a wide band around the Fermi energy are effectively absorbed [168]. As a rule of thumb, one can choose the potential height to be the location of the Fermi energy, E_F, above the bottom of the calculated valence band, E_0, $V_0 \approx E_F - E_0$. The width of the potential should be sufficiently larger than the Fermi wavelength. For example, the width for a carbon wire is taken to be $\sigma \approx 20a_0$, where a_0 is Bohr's radius. The origin of the potential $z_0^{L(R)}$ is chosen such that the region of the lead close to the device where the effect of the potential is negligible contains at least a few Fermi wavelengths such that the metallic nature of the lead is appropriately captured. This choice of parameters should serve as an initial try and a convergence check should then be conducted. The Gaussian absorbing potential is, of course, not a unique choice and other forms of absorbing potential expressions can be used [169].

Within the absorbing potentials methodology the system is not divided into sub-units and the dimensionality of all the matrices appearing in equation (24) is the dimensionality of the full system (device+truncated leads). The $\Gamma_{L(R)}$ matrix elements are calculated (usually numerically) as integrals of the atomic basis functions over the imaginary potential $V_{L(R)}$. It should be noted that, similar to the WBL discussed above, the Γ matrices in the current methodology are energy-independent. This fact considerably reduces the computational efforts involved in the evaluation of the transmission probability.

The device GF in equation (24) is now replaced by the GF of the whole system which, similar to equation (29), is given by

$$\hat{G}^r(E) = \left[E\hat{S} - \hat{H} - i\hat{\Gamma}_L - i\hat{\Gamma}_R\right]^{-1}, \tag{36}$$

where $\hat{S}$ and $\hat{H}$ are the overlap and Hamiltonian matrices, respectively, calculated for the whole system, and E is the real energy. The advanced GF is, as before, the Hermitian conjugate of the retarded counterpart $G^a(E) = [G^r(E)]^\dagger$.

The last remaining task for the calculation of the conductance is the calculation of the Hamiltonian, overlap and coupling matrices appearing in equation (28). This calculation is explained in the next section.

4.4. Electronic structure—tight binding magnetic extended Hückel theory

The final task before performing the calculations of the conductance is the appropriate representation of the electronic structure of the system under the influence of the external magnetic field. For this purpose, a tight binding magnetic extended Hückel theory (TB-MEHT) was developed. This approach provides a description of the Hamilton matrix elements as well as the corresponding basis set. Thus, it can be used to include the effects of external perturbations such as magnetic fields by simply incorporating these into the Hamiltonian and evaluating the perturbation matrix elements with the given basis.

Spin effects, which have been considered mainly for mesoscopic AB interferometers utilizing spin–orbit couplings [170–181, 142, 182], are ignored here. Since molecular rings lack a Rashba/Dresselhaus [183, 184] field leading to spin–orbit coupling, and since one is interested in small magnetic fields where the Zeeman spin splitting is negligible [145], it is safe to ignore the spin degree of freedom for the present application. For a recent discussion of molecular spintronic devices utilizing an AB interferometer, see [145].

Consider the one-body electronic Hamiltonian of the form

$$\hat{H} = \frac{1}{2m_e}\left[\hat{\mathbf{P}} - q\mathbf{A}\right]^2 + V(\mathbf{r}). \tag{37}$$

The notation used here is similar to that used for the Hamiltonian presented in equation (1). Within the TB-MEHT formalism the contribution at zero vector potential, $\hat{H}(\mathbf{A} = \mathbf{0}) = \frac{\mathbf{P}^2}{2\mathbf{m}} + \mathbf{V}(\mathbf{r})$, is represented by the tight binding extended Hückel (TB-EH) Hamiltonian $\hat{H}^{EH}$ [185], which approximates the complex many-body problem using a mean-field, single-particle, semi-empirical approach. The effect of applying a vector potential is taken into account by simply adding the appropriate magnetic terms to the EH Hamiltonian:

$$\hat{H} = \hat{H}^{EH} - \frac{q}{2m_e}\left(\hat{\mathbf{P}}\cdot\mathbf{A} + \mathbf{A}\cdot\hat{\mathbf{P}}\right) + \frac{q^2}{2m}A^2. \tag{38}$$

As before we assume that the magnetic field is uniform and constant, $\mathbf{B} = (B_x, B_y, B_z)$, and thus write down the related vector potential as: $\mathbf{A} = -\frac{1}{2}\mathbf{r}\times\mathbf{B} = -\frac{1}{2}(yB_z - zB_y, zB_x - xB_z, xB_y - yB_x)$. Putting this expression in equation (38) one obtains the following electronic Hamiltonian [186]:

$$\hat{H} = \hat{H}^{EH} - \frac{\mu_B}{\hbar}\mathbf{L}\cdot\mathbf{B} + \frac{q^2\mathbf{B}^2}{8m_e}\mathbf{r}_\perp^2. \tag{39}$$

Here, $\mu_B = \frac{q\hbar}{2m_e}$ is the Bohr magneton, $\mathbf{r}_\perp^2 = \mathbf{r}^2 - \frac{(\mathbf{r}\cdot\mathbf{B})^2}{\mathbf{B}^2}$ is the projection of $\mathbf{r} = (x, y, z)$ onto the plane perpendicular to $\mathbf{B}$ and $\hat{\mathbf{L}} = \mathbf{r}\times\hat{\mathbf{P}}$ is the angular momentum operator.

For the sake of simplicity, and without limiting the generality of the solution, we assume that the AB ring is placed in the Y–Z plane and that the magnetic field is applied parallel to the X axis. With this, the Hamiltonian in equation (39) is reduced to

$$\hat{H} = \hat{H}^{EH} + i\mu_B B_x\left(y\frac{\partial}{\partial z} - z\frac{\partial}{\partial y}\right) + \frac{q^2B_x^2}{8m_e}(y^2 + z^2). \tag{40}$$

A Slater-type orbital (STO) [187, 188] basis set is used to evaluate the Hamiltonian and overlap matrices. In the presence of a magnetic field it is necessary to multiply each STO by an appropriate gauge factor which compensates for the finite size of the set. The resulting atomic orbitals are customarily referred to as gauge-invariant [189, 190] Slater-type orbitals (GISTOs) and are given by

$$|\overline{n,l,m}\rangle_\alpha = \mathrm{e}^{\frac{\mathrm{i}q}{\hbar}\mathbf{A}_\alpha\cdot\mathbf{r}}|n,l,m\rangle_\alpha = \mathrm{e}^{\frac{\mathrm{i}qB_x}{2\hbar}(y_\alpha z - z_\alpha y)}|n,l,m\rangle_\alpha. \quad (41)$$

Here $|n,l,m\rangle_\alpha$ is an STO characterized by the set of quantum numbers (n,l,m), and centered on the atomic site α. $\mathbf{A}_\alpha$ is the value of the vector potential $\mathbf{A}$ at the nuclear position $\mathbf{R}_\alpha = (x_\alpha, y_\alpha, z_\alpha)$ and $|\overline{n,l,m}\rangle_\alpha$ is the GISTO situated at α.

The generalized eigenvalue problem $\overline{\hat{H}}\psi_n = E_n\overline{\hat{S}}\psi$ is solved to get the electronic energy levels (E_n) and the molecular orbitals (ψ_n) characterizing the system. Here, $\overline{\hat{H}}$ and $\overline{\hat{S}}$ are the Hamiltonian and overlap matrices with elements given by $\overline{\hat{S}}_{1\alpha,2\beta} =_\alpha \langle\overline{n_1,l_1,m_1}|\overline{n_2,l_2,m_2}\rangle_\beta$ and $\overline{\hat{H}}_{1\alpha,2\beta} =_\alpha \langle\overline{n_1,l_1,m_1}|\hat{H}|\overline{n_2,l_2,m_2}\rangle_\beta$. The London approximation [189, 190] is used to calculate the different matrix elements. Within this approximation the gauge phase appearing in equation (41) is taken outside the integral, replacing $\mathbf{r}$ by $\frac{1}{2}(\mathbf{R}_\alpha + \mathbf{R}_\beta)$. The overlap integrals are then given by

$$\overline{\hat{S}}_{1\alpha,2\beta} \approx \hat{S}_{1\alpha,2\beta}\mathrm{e}^{\mathrm{i}L_{\alpha\beta}}. \quad (42)$$

Here, $\hat{S}_{1\alpha,2\beta} =_\alpha \langle n_1,l_1,m_1|n_2,l_2,m_2\rangle_\beta$ and $L_{\alpha\beta} = \frac{q}{2\hbar}(\mathbf{A}_\beta - \mathbf{A}_\alpha)\cdot(\mathbf{R}_\alpha + \mathbf{R}_\beta) = \frac{qB_x}{2\hbar}(z_\alpha y_\beta - y_\alpha z_\beta)$. The Hamiltonian matrix elements are approximated as

$$\overline{\hat{H}}_{1\alpha,2\beta} \approx \tfrac{1}{2}\left[\hat{H}_{1\alpha,2\beta}\mathrm{e}^{\mathrm{i}L_{\alpha\beta}} + \hat{H}_{1\beta,2\alpha}\mathrm{e}^{\mathrm{i}L_{\beta\alpha}}\right], \quad (43)$$

where $\hat{H}_{1\alpha,2\beta} =_\alpha \langle n_1,l_1,m_1|\hat{H}|n_2,l_2,m_2\rangle_\beta$. This form guarantees that the Hamiltonian matrix remains Hermitian under the approximation.

All matrix elements in the formulation presented above are calculated analytically. The EH Hamiltonian diagonal matrix elements are set to be equal to the ionization potentials of the appropriate atomic orbital, $\hat{H}^{\mathrm{EH}}_{1\alpha,1\alpha} = I.P._{1\alpha}$, while the off-diagonal elements are given by an average of the corresponding diagonal elements: $\hat{H}^{\mathrm{EH}}_{1\alpha,2\beta} = k\frac{\hat{H}^{\mathrm{EH}}_{1\alpha,1\alpha}+\hat{H}^{\mathrm{EH}}_{2\beta,2\beta}}{2}\hat{S}_{1\alpha,2\beta}$, where $k = 1.75$ is a parameter chosen to give the best fit to experimental data. The overlap matrix is calculated analytically for every set of quantum numbers using a method developed by Guseinov *et al* [191–195]. The matrix elements of the magnetic terms appearing in the Hamiltonian can then be expressed as a linear combination of overlap integrals and are thus also calculated without the need to perform numerical integration. The expansion of the magnetic integrals in terms of corresponding overlap integrals is presented elsewhere [196].

Before continuing, it should be mentioned that, while the current model does take into account the explicit geometry of the system and also some of the details of the system's electronic structure, it remains an effective one-particle model and neglects contributions from electron–electron correlations and coupling to the vibrational degrees of freedom of the molecular device. Furthermore, since the bias potential is assumed to drop sharply at the lead–device junctions and its effect on the energy levels of the device is neglected, the current model is valid only at the low bias regime.

4.5. Results for two-terminal devices

In the present section we study the magnetoresistance behavior of two-terminal devices as a function of the relevant physical control parameters identified in section 3.1. The atomistic calculations are compared to those obtained using the continuum model.

4.5.1. Atomic corral. First, we consider a corral composed of monovalent atoms placed on a semi-conducting surface and coupled to two atomic wires. An experimental realization of this set-up can be achieved using scanning tunneling microscopy (STM) techniques [197–200]. The whole set-up is then placed in a perpendicular homogeneous and constant magnetic field and the conductance between the atomic wire leads through the corral is measured, at the limit of zero bias voltage, as a function of the threading magnetic field. Realizing that the corral itself is also constructed of an atomic wire it is important to understand some basic properties of such one-dimensional structures.

Since each atomic site contributes a monovalent electron, the number of atoms in the chain, N, must be even to get a closed shell wire. The Fermi energy of the wire has a principal quantum number of $\frac{N}{2}$, which is also the number of nodes the Fermi electrons wavefunctions have. If the distance between the atomic sites, d, is constant then the separation between the nodes is given by $\frac{Nd}{N/2} = 2d$ and thus the Fermi wavelength is $\lambda_{\mathrm{F}} = 2\times 2d = 4d$. Therefore, one sees that, for any regular atomic wire composed of monovalent atomic sites, the conducting electrons' wavelength is of the order of four interatomic distances. This simple conjecture allows us to divide the symmetric atomic corrals into two prototypes: those having $N = 4n$ and those having $N = 4n+2$ atoms on the circumference, where n is an integer number. For an $N = 4n$ atomic corral the quantum number of the Fermi wavefunction of a particle on a ring is an integer: $m_{\mathrm{F}} = k_{\mathrm{F}}r = \frac{2\pi}{\lambda_{\mathrm{F}}}\frac{Nd}{2\pi} = \frac{Nd}{4d} = \frac{N}{4} = n$, and therefore the resonance condition in equation (11) is obtained when the magnetic field is off. However, when $N = 4n+2$, one obtains $m_{\mathrm{F}} = n + \frac{1}{2}$ and resonance is achieved only when $\frac{\phi}{\phi_0} = \frac{l}{2}$ where $l = \pm1, \pm2, \ldots$.

A similar picture arises when plotting the wavefunctions of the Fermi electrons. The complex normalized wavefunctions of a particle on a ring are given by: $\Psi_{\pm m}(\theta) = \frac{1}{\sqrt{2\pi}}\mathrm{e}^{\pm\mathrm{i}m\theta}$. A linear combination of each doubly degenerate functions having the same quantum number m results in real wavefunctions of the form $\frac{1}{\sqrt{\pi}}\cos(m\theta)$ and $\frac{1}{\sqrt{\pi}}\sin(m\theta)$. The cosine functions are plotted in panels (a) and (b) of figure 11 for the two corral prototypes having $m = m_{\mathrm{F}} = \frac{N}{4}$.

As can be seen, for the $4n$ prototype a standing wave is obtained for which both input and output leads are located at non-stationary points. For the $4n+2$ corral at zero magnetic flux the wavefunction is not stationary and the output lead

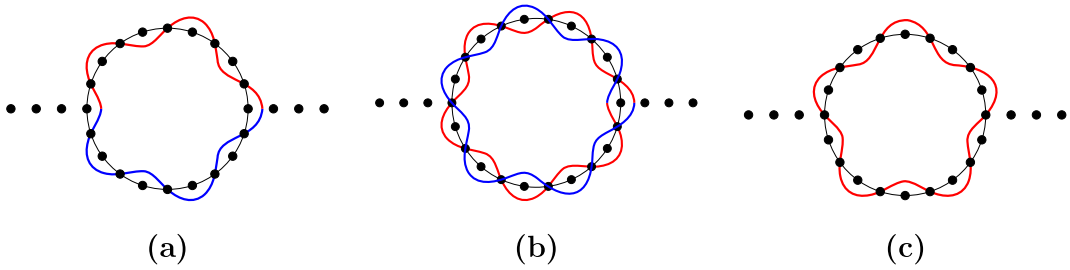

Figure 11. An illustration of the Fermi wavefunctions of a particle on a ring-shaped corral. Panel (a): a cosine wavefunction for a $4n$ ring with $n = 5$ creates a stationary solution. Panel (b): a cosine wavefunction of a $4n + 2$ ring with the same n as before creates a destructive interference between the clockwise (blue) and counterclockwise (red) electron pathways. Panel (c): a sine wave functions for $N = 4n$ atoms with $n = 5$.

is located exactly at a node of the interference between the clockwise and counterclockwise traveling electrons. In fact, the interference is destructive not only at the nodes but for every point on the ring and thus this energy level does not exist. It is interesting to note that the sine function, which is shifted by $\frac{\pi}{2}$ from the cosine counterpart, has both leads located at its nodes, as can be seen in figure 11(c). Therefore, at a given leads' location and in the absence of a gate potential and a magnetic field only one of the two degenerate energy levels will conduct and the maximum zero bias conductance will be the quantum conductance, g_0.

An alternative explanation for this class division can be given based upon the energetic structure of the ring. Due to the symmetry of the ring, apart from the lowest energy level, all energy levels of a particle on an uncoupled ring are doubly degenerate. When considering a monovalent electron per site corral the occupation of the energy levels of the $4n$ prototype differs from that of the $4n + 2$ prototype.

This can be seen in figure 12 where the highest occupied molecular orbital (HOMO) occupation is presented for both prototypes. The HOMO occupation of the $4n$ prototype (left panel) involves two vacancies and thus is suitable for electron conduction when brought to resonance with the leads, while the HOMO occupation of the $4n + 2$ prototype (right panel) is full and therefore does not conduct electrons.

After realizing these important features of one-dimensional monovalent atomic wires, we turn to present atomistic calculations results obtained using the imaginary potentials method within the TB-MEHT formalism as discussed above. In figure 13 the conductance through atomic corrals composed of 40 and 42 copper atoms is plotted [111]. All atoms on the corral are separated by a distance of 2.35 Å. The effect of a gate potential was simulated by changing the corral atomic orbital energies by V_g.

As discussed above, at zero gate voltage the conductance peak for the $n = 40$ corral is located at the low magnetic field region while for the $n = 42$ corral it is located near the middle of the AB period. Two common features are clearly observed for the two corral prototypes: (a) a large magnetic field (∼500–600 T) is required to complete a full AB period and (b) the conductance peaks (red spots) shift with the gate voltage, V_g. The latter effect is analogous to the shift of peaks seen in figure 5 for the continuum model as the conducting electron wavenumber is varied. Therefore, the application of

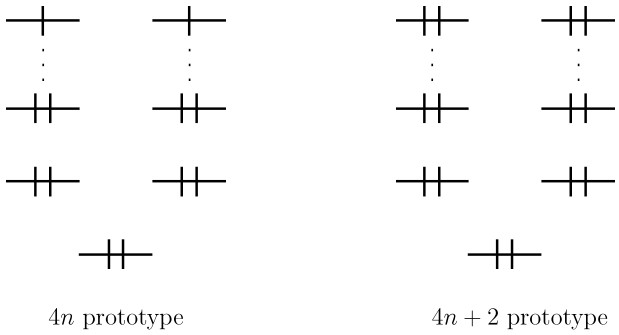

Figure 12. The occupation of the energy levels of the corral for the $4n$ prototype (left panel) and for the $4n + 2$ prototype (right panel).

a gate voltage allows control over the location of the peak conductance. In particular, it can be used to shift the maximal conductance to zero magnetic field for the $N = 4n + 2$ corral prototype and to fine tune the location of the $N = 4n$ peak if slightly shifted from the magnetic field axis origin.

The next step is to control the width of the conductance resonances as a function of the magnetic field. In the continuum model, this was done by reducing the transmission amplitude, ϵ. In the molecular system this can be achieved by increasing the distance between the ring and the edge lead atom closest to the ring. Alternatively, one can introduce an impurity atom at the junctions between the lead and the ring. However, for quantum corrals the former approach seems more realistic.

In figure 14 the conductance as a function of the magnetic field is depicted for several values of the lead–ring separation. For each generic corral prototype, an appropriate gate voltage is applied to ensure maximal conductance at $B = 0$ T. As the lead–ring separation is increased, the lifetime of the energy levels on the ring is increased and therefore their width decreases. This is translated into a sharpening of the switching response to the magnetic field in the magnetoconductance spectrum. At the highest separation studied one achieves a switching capability of the order of a *single tesla*, despite the fact the AB period is comparable to 500–600 T.

Due to the dependence of the AB period on the magnetic flux, the effects discussed above are scalable with the dimension of the ring, as long as the simple physics holds. For a given lead–corral coupling strength, doubling the cross section of the corral will reduce the switching limit to half

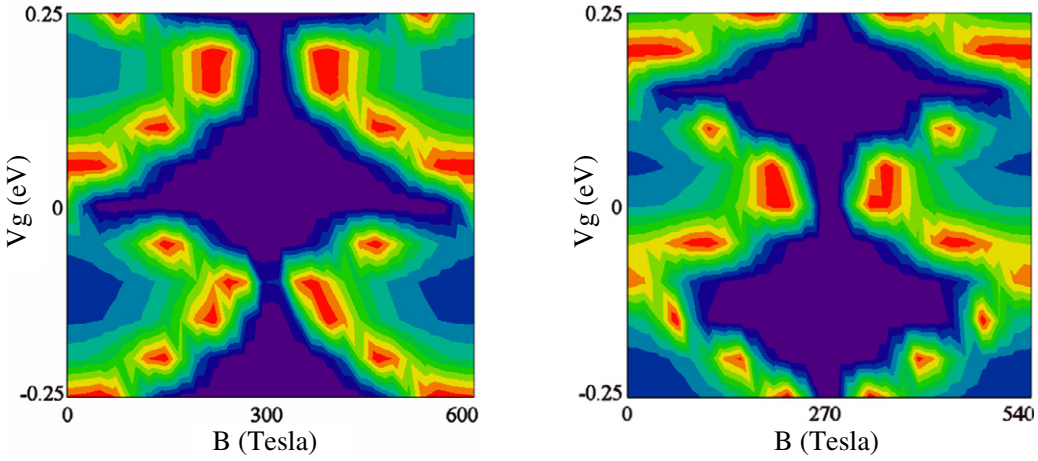

Figure 13. Conductance as a function of the magnetic field and the gate voltage for a 40 (left panel) and a 42 (right panel) atomic corral composed of copper atoms at $T = 1$ K. Color code: red—$g = g_0$, purple—$g = 0$.

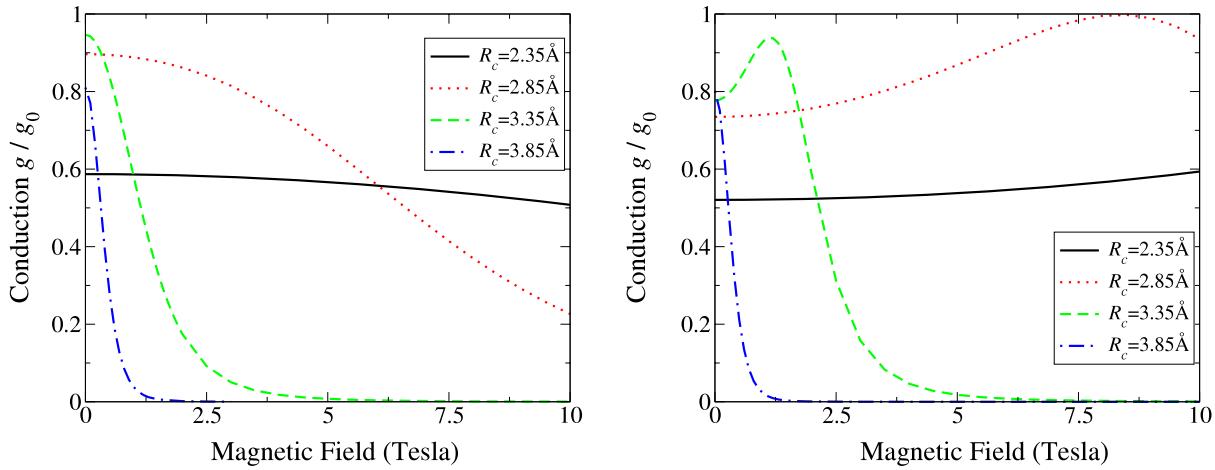

Figure 14. Conductance as a function of the magnetic field and the contact bond length (R_c) for a 40 (left panel) and a 42 (right panel) atomic corral composed of copper atoms at $T = 1$ K. The gate potential is 0 V (left) and −0.132 V (right).

its original value for a given lead–device coupling at low enough temperatures. This can be clearly seen in figure 15, where the magnetoconductance of several corrals with inter-site spacing of 1 Å and at a temperature of 1 K is calculated in the WBL with a coupling strength of 0.05 eV. For a corral with a diameter of ∼1.3 nm switching occurs at ∼4 T (solid curve in the figure). When doubling the diameter of the corral (multiplying the cross section by 4) the switching threshold reduces to ∼1 T (dashed line in the figure), as expected. Upon a further increase in the dimensions of the corral (dashed–dotted line) the switching threshold reduces respectively.

4.5.2. Carbon nanotubes. Another interesting (and perhaps somewhat more accessible experimentally) system is an AB interferometer based on a carbon nanotube (CNT) [201]. CNTs have been investigated in the context of molecular electronics both experimentally [48, 52, 53, 131, 202–205, 55, 206, 132, 133] and theoretically [207–209]. The AB effect in single-walled and multi-walled carbon nanotubes (SWCNT and MWCNT, respectively) has been addressed experimentally and theoretically as well [210–219] (for a recent review, see [220]). These studies focus on the AB effect in CNTs, while in this review we describe the conditions for which switching can be obtained at magnetic fields that are much smaller than those corresponding to a full AB period in CNTs [112].

Similar to the quantum corral set-up, when a magnetic field is applied perpendicular to the cross section of the tube (along its main axis), electron pathways traversing the circular circumference in a clockwise and a counterclockwise manner gain different magnetic phases, and thus AB interference occurs. As the coupling between the CNT and the conducting leads is decreased, a resonant tunneling junction forms. This results in an increase of the electron's lifetime on the CNT and thus in a narrowing of the energy levels' width. Using a bias/gate potential it is possible to tune the resonance such that the transmittance is high at zero magnetic field. The application of low magnetic fields shifts the narrow energy level out of resonance. Thus switching occurs at fields much smaller than those required to achieve a full AB cycle.

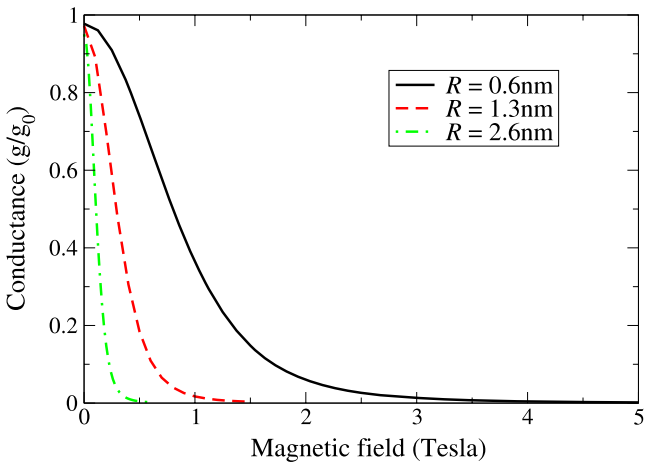

Figure 15. Magnetoconductance through an atomic corral as a function of the corral dimensions. As the diameter of the corral is doubled from ∼1.3 nm (solid line) to ∼2.6 nm (dashed line) the switching threshold reduces by a factor of 4. For the largest corral considered (dashed–dotted line) the switching threshold is ∼0.5 T for a coupling strength of 0.05 eV.

Two different experimental configurations are considered for this purpose [112]. The first consists of an SWCNT placed on an insulating substrate between two thin conducting contacts (see figure 16(a)) and a bias potential is applied between the contacts. Similar set-ups have been recently demonstrated experimentally [30, 221–223]. In the second configuration an SWCNT is placed on a conducting substrate coupled to a scanning tunneling microscope (STM) tip from above as described schematically in figure 16(b). The bias potential is applied between the STM tip and the underlying surface. For both configurations the resulting conductance between the leads can be calculated using the TB-MEHT approach described above, showing that high sensitivity to the magnetic field can be achieved.

For configuration (a) (figure 16(a)) both leads are modeled by atomic conducting wires and the calculations are done using the imaginary potentials method (see section 4.3), while for configuration (b) (figure 16(b)) the STM tip is modeled by a semi-infinite one-dimensional atomic conducting gold wire and the substrate is modeled by a semi-infinite slab of gold crystal. The iterative procedure discussed in section 4.2 was applied to obtain the semi-infinite bulk Green's function. The calculations were conducted for a tube four unit cells in length, using minimum image periodic boundary conditions for the passivation of the edge atoms. Such short CNTs have been recently synthesized [224]. Tests on longer tubes reveal the same qualitative picture described below.

The density of states on a 1.6 nm long $(24, 0)$ SWCNT segment is plotted in figure 17. A sketch of the short segment of the SWCNT is shown in the inset of the figure. Two doubly degenerate energy levels appear in near the Fermi energy, which are separated from the rest of the spectrum by approximately 100 meV. Resonant tunneling through these states accompanied by degeneracy lifting due to the Aharonov–Bohm effect allows for delicate control over the conductance through the system.

In figure 18, the conductance through the cross section of the $(24, 0)$ SWCNT segment, as calculated for configuration (a), is plotted against the external axial magnetic field for several bias potentials. The conductance at zero bias first increases as one switches on the magnetic field (negative magnetoresistance), peaks near $B = 10$ T and subsequently decreases as the field grows, vanishing at fields above 30 T. The maximum conductance observed, $g/g_0 = 2$, is limited by the number of open channels in the vicinity of the Fermi energy of the SWCNT. In order to achieve switching capability at magnetic fields smaller than 1 T, it is necessary to move the conductance peak to zero magnetic fields and, at the same time, reduce its width.

When a small bias is applied to the sample the conductance peak splits into a doublet[6]. The position of the corresponding peaks depends on the value of the bias and the maximum conductance is reduced by 25%–50%. As can be

[6] This is due to the specific way one may chose the bias potential drop at the two lead–device junctions as described in section 4.1. For different bias potential profiles the quantitative details of the calculations would change however, the qualitative picture would remain the same.

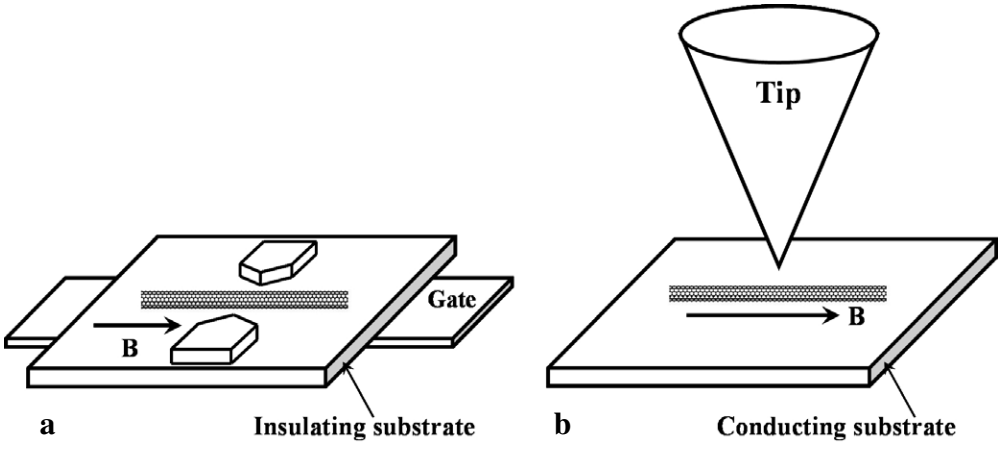

Figure 16. An illustration of the experimental configurations suggested for measuring the cross-sectional magnetoresistance of a CNT. In configuration (a) the SWCNT is placed on an insulating surface between two narrow metallic contacts, while in configuration (b) the SWCNT is placed on a conducting substrate and approached from above by an STM tip.

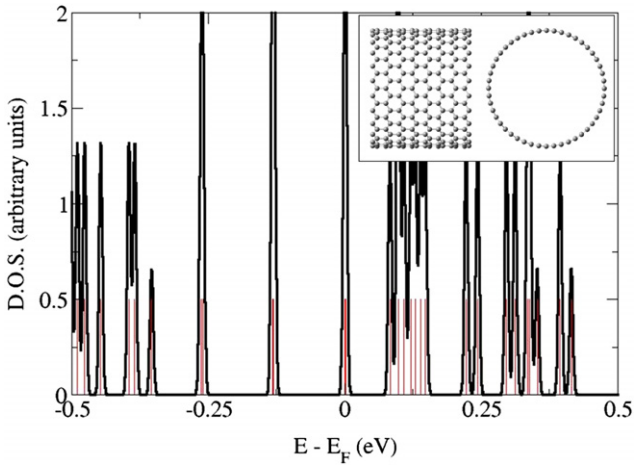

Figure 17. Density of states in the vicinity of the Fermi energy as calculated by the TB-MEHT for a (24, 0) SWCNT segment. Lighter coloured lines indicate the position of the energy levels. Gaussian broadening of 0.08 eV was introduced for clarity. Inset: axial and side views of the 1.6 nm long (24, 0) SWCNT segment.

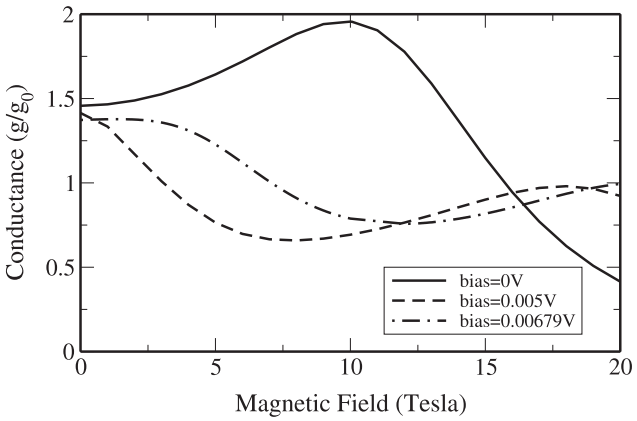

Figure 18. Conductance versus the magnetic field for several bias potentials as calculated by the TB-MEHT for a (24, 0) SWCNT placed as in configuration (a). The effect of the application of a bias potential on the position of the conductance peaks is depicted at a constant tube–contact separation of 2.4 Å.

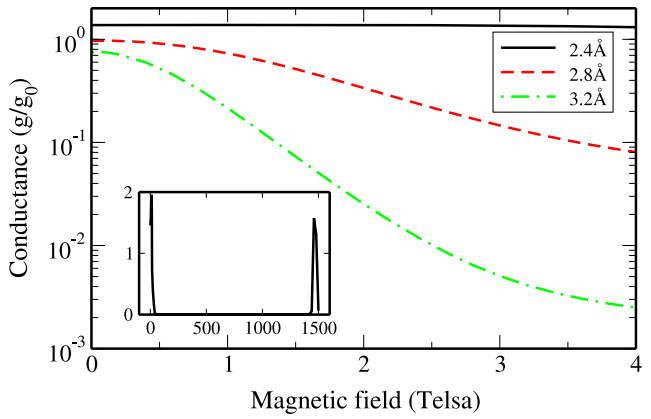

Figure 19. Conductance versus the magnetic field for several tube–contact separations as calculated by the TB-MEHT for a (24, 0) SWCNT placed as in configuration (a). The effect of an increase in the tube–contact separation is depicted at a constant bias potential of 0.00679 V. Inset: the full AB period for a (24, 0) SWCNT at zero bias potential and tube–contact separation of 2.4 Å.

seen in the figure, by adjusting the bias potential it is possible to shift one of the conductance peaks toward low values of the magnetic field, such that the conductance is maximal at $B = 0$ T and positive magnetoresistance is achieved. The shift in the conductance peak can be attributed to the change in the energy level through which conductance occurs when a small bias is applied. As a result of this change, the electron momentum is altered, resulting in the conductance peak shift observed in the calculation.

In figure 19, the effect of changing the tube–contact separation at constant bias potential is studied. As one increases the separation between the tube and the contacts, their coupling decreases, resulting in a reduction of the width of the energy resonances of the SWCNT. Thus, the conductance becomes very sensitive to an applied magnetic field and small variations in the field shift the relevant energy level out of resonance. In the magnetoresistance spectrum, this is translated to a narrowing of the transmittance peaks, similar to the case of the atomic corral discussed in section 4.5.1. For the smallest separation considered (2.4 Å), the conductance seems to be constant, on the logarithmic scale, at the magnetic field range shown in the figure, while at the highest separation studied (3.2 Å), the width of the conductance peak is comparable to 1 T. At higher magnetic fields (not shown) the conductance of the 2.4 Å case reduces as well.

Similar to the corral case, the combined effect of the bias potential and the tube–contact separation allows us to shift the position of the conductance peak to small magnetic fields while at the same time reducing its width. This is achieved by carefully selecting the values of the bias potential and tube–contact separation. Under proper conditions, one obtains positive magnetoresistance with a sharp response occurring at magnetic fields comparable to 1 T. This result is significant since it implies that, despite the fact that the tube radius is small (∼1 nm) and the corresponding full AB period requires unrealistically large magnetic fields of the order of 1500 T (as shown in the inset of figure 19), it is possible to achieve magnetic switching at relatively small magnetic fields.

A similar picture arises when considering configuration (b). In figure 20 we show the conductance as calculated for a (6, 0) SWCNT placed between a sharp STM tip and a conducting surface for two bias voltages. A smaller-diameter CNT was used in these calculations in order to be able to properly describe the bulky nature of the conducting substrate with respect to the dimensions of the CNT.

As can be seen, when a bias voltage of ∼0.224 V is applied the conductance peaks at a magnetic field of ∼14 T. By changing the bias potential to ∼0.225 V the conductance peak shifts toward zero magnetic field. Under these conditions switching occurs at a magnetic field of ∼10 T while the full AB period for this system is of the order of 2×10^4 T. The CNT–lead separation required to achieve high magnetoresistance sensitivity in this configuration is larger than the one needed

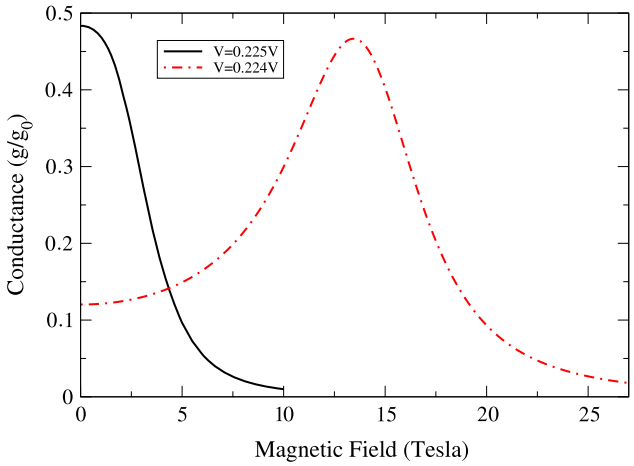

Figure 20. Conductance as a function of the magnetic field through a (6, 0) CNT as calculated for configuration (b) at different bias voltages. The separation between the CNT and the conducting leads used in this calculation is taken to be 4.1 Å.

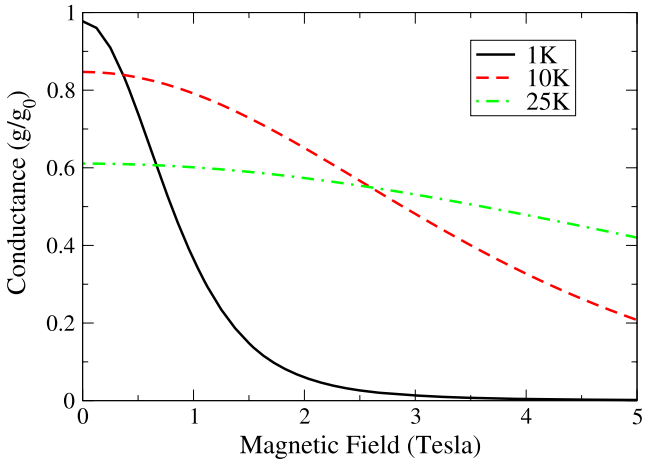

Figure 21. Magnetoconductance through an atomic corral composed of 40 single-electron sites with 1 Å spacing at different temperatures. It can be seen that, as the temperature rises from 1 K (solid line) to 10 K (dashed line), the device response becomes less sensitive to the magnetic field. At 25 K (dashed–dotted line) the conductivity is almost insensitive to the magnetic field at the low magnetic field region.

for configuration (a). This is due to the difference in the CNT diameters and the different lead geometries. As the diameter of the tube becomes smaller, the magnetic field needed to gain a similar AB phase shift grows larger. Therefore, the conductance peaks become wider so that larger CNT–lead separations are required in order to narrow their width. Furthermore, as the lead becomes more bulky its coupling to the CNT needs to be decreased in order to achieve the same magnetoresistance sensitivity.

To conclude the CNT AB interferometry part, it was shown that SWCNTs can be used as magnetoresistance switching devices based on the AB effect. As in the corral set-up, the essential procedure involves the weak coupling of the SWCNT to the conducting leads in order to narrow the conducting resonances, while at the same time controlling the position of the resonances by the application of a bias potential. The control over the coupling between the SWCNT and the conducting leads in configuration (a) of figure 16 can be achieved via a fabrication of a set of leads with proper gaps. In configuration (b) of the same figure one needs to control the distance between the STM tip and the CNT and between the substrate and the CNT. The former can be achieved by piezoelectric control and the latter by covering the surface with monolayer/s of an insulating material.

4.5.3. Operative limitations. The above calculations have been performed assuming a low temperature of 1 K (apart for the (6, 0) CNT where a temperature of 0.1 K was used). However, the effect will hold even at higher temperatures. Recall that, within the Landauer formalism, the temperature effect is taken into account only through the difference of the leads' Fermi–Dirac population distributions $f_{\mathrm{L(R)}}(E, \mu_{\mathrm{L(R)}})$. This difference sets the (temperature-dependent) width of the energy band through which conductance occurs. Thus, this width should be narrow enough (the temperature should be low enough) in order to resolve the magnetic field splitting of the, originally degenerate, energy levels of the ring. Using equation (11), one finds that this splitting is given by $\frac{\hbar^2}{2m^\star R^2}[(-|m_{\mathrm{F}}| - \frac{\phi}{\phi_0})^2 - (|m_{\mathrm{F}}| - \frac{\phi}{\phi_0})^2] = \frac{2\hbar^2 m_{\mathrm{F}}}{m^\star R^2}\frac{\phi}{\phi_0} = \frac{2\hbar^2 k_{\mathrm{F}}}{m^\star R}\frac{\phi}{\phi_0}$. Therefore, the temperature should fulfill the following condition in order for AB switching to be observed: $k_{\mathrm{B}}T < \frac{2\hbar^2 k_{\mathrm{F}}}{m^\star R}\frac{\phi}{\phi_0}$.

Considering an atomic corral with a diameter of ∼1.3 nm and interatomic distances of 1 Å (40 atomic sites), the normalized magnetic flux at 5 T is $\frac{\phi}{\phi_0} \approx 1.5 \times 10^{-3}$ and the Fermi wavelength is $\lambda_{\mathrm{F}} \approx 4$ Å, resulting in a Fermi wavenumber of $k_{\mathrm{F}} = \frac{2\pi}{\lambda_{\mathrm{F}}} \approx \frac{\pi}{2}$ Å^{-1}. Assuming an effective mass of $m^\star = 1$ au one gets an upper limit of approximately 7 K.

This can be seen in figure 21 where the magnetoconductance through such a corral is calculated using the WBL at different temperatures. The coupling to both leads is taken to be 0.05 eV such that switching occurs at ∼5 T. As the temperature rises from 1 K (solid curve in the figure) to 10 K (dashed line in the figure) the device response becomes less sensitive to the magnetic field even though an effect is still observable, as predicted. At a higher temperature of 25 K (dashed–dotted line) the conductivity becomes almost insensitive to the magnetic field at the magnetic field region considered.

4.6. Results for three-terminal devices

As discussed in section 3.2, an interesting case in which magnetic fields provide unique control over the conductance is based on the three-terminal set-up. Here, we describe an example based on a polycyclic aromatic hydrocarbon (PAH) [113]. A sketch of such a ring composed of 48 conjugated benzene units with a diameter of ∼3 nm is shown in figure 22. Similar PAH molecules have been synthesized by chemical means [225–227] and studied theoretically [228–231]. This structure can also be viewed as

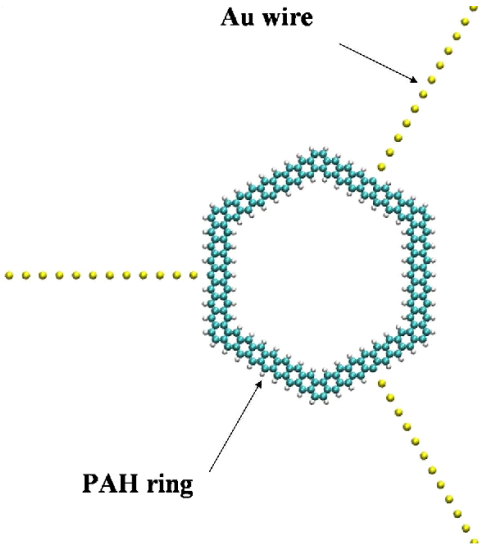

Figure 22. A realization of a three-terminal molecular AB interferometer based on a polycyclic aromatic hydrocarbon molecule coupled to three atomic gold wires.

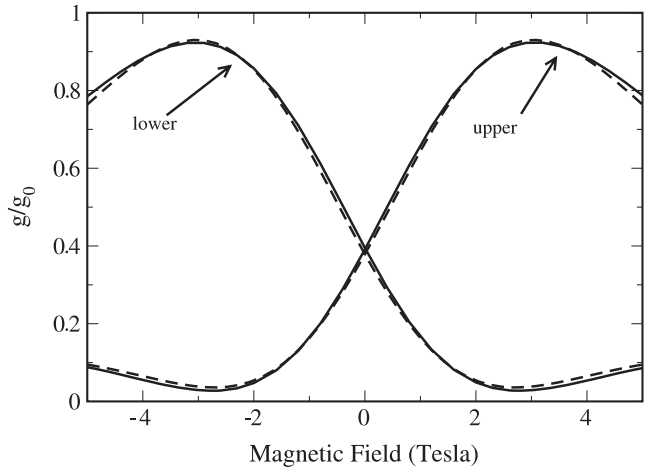

Figure 23. Magnetoconductance of the three-terminal molecular device shown in figure 22. Solid lines correspond to the conductance of the upper and lower outgoing terminals calculated by TB-MEHT formalism. Dashed lines correspond to the conductance of the upper and lower outgoing terminals calculated by the continuum model.

a closed form of a graphene nanoribbon [61, 64, 66, 110], a class of materials that has attracted a great deal of theoretical activity recently [232–237].

In figure 23 we show the zero bias conductance of the molecular switch as a function of the magnetic field intensity for both output channels. We focus on the region of realistic magnetic fields (much smaller than the field required to complete a full AB period which is ∼470 T for a ring with a cross-sectional area of about 8.75 nm^2). A relatively large gate voltage, $V_g = 1.85$ V, is needed in order to bring the system into resonance, and the lead–molecule separation is taken to be ∼3 Å.

For zero magnetic field, both channels are semi-opened and the conductance assumes a value of $0.4g_0$ at the selected gate voltage. When a magnetic field of ∼2.5 T is applied, one finds that one output channel fully opens while the other closes shut. As the polarity of the field changes sign the two output channels interchange their role. Exactly the same characteristics are captured by the continuum model (e.g. dashed lines in figure 23). Therefore, it can be seen that the magnetic field polarity serves as a distributor that streams the electrons to the desired output channel.

Based on this magnetic rectification behavior, it is possible to design a molecular logic gate, which processes two different logic operations simultaneously. This can be achieved by choosing one input signal as the bias voltage (V_b) and the other input signal as the magnetic field (B). For the bias input signal, V_b, we mark as '0' the case where $V_b = 0$ V and as '1' the case where a small bias is applied. For the magnetic field input signal we mark as '0' the case where $B \approx -3$ T and as '1' the case where $B \approx 3$ T. The output signals are the currents measured at the two outgoing leads marked as I_1 and I_2. Using these definitions the truth table presented in table 1 can be constructed.

One sees that the output I_1 gives the logic operation V_b && B while the output O_2 gives the logic operation

Table 1. Truth table for the parallel molecular logic gate.

V_b	B	I_1	I_2
0	0	0	0
0	1	0	0
1	0	0	1
1	1	1	0

V_b && $\overline{B}$ where the overbar stands for NOT. Even though the conductance peaks are sharp relative to the full AB period, this truth table holds for a wide range of the threading magnetic field intensity ±(2–4) T and is thus suitable for robust logic gate operations. Shifting the conductance peaks via the change of the gate potential will give rise to different logic operations of the same set-up.

To summarize the current section, it can be seen that single cyclic molecules are promising candidates for the fabrication of magnetoresistance parallel switching and gating devices at feasible magnetic fields. As in the previous discussion, careful fine tuning of experimentally controllable physical parameters allows the selective switching of a single pre-selected output channel, thus allowing for the design of a molecular logic gate, processing two logic operations in parallel. This is made possible due to the unique symmetry breaking nature of the magnetic gate.

5. Inelastic scattering effects in AB molecular interferometers

Our discussion above neglects completely inelastic effects arising from electron–phonon couplings (EPCs). Such processes have been considered in molecular junctions by several authors utilizing different theoretical approaches [238–243, 165, 244–248]. In AB interferometers, EPC were considered in mesoscopic rings, where EPC leads to a decay in the amplitude of the AB oscillations [249] and more recently in the context of

electron–electron interaction [250]. In this section we address the issue of inelastic effects arising from EPCs for molecular AB interferometers where we focus on the low magnetic flux regime, as appropriate for such systems [114]. We show, as expected, that the EPC *broadens* the conduction peak when an electric gate is applied [244]. In contrast, dephasing processes arising from EPC *narrow* the magnetoconductance response and thus increase the sensitivity to the threading magnetic flux. This surprising result can be rationalized in terms of a rapid loss of the phase of electrons at the exit channel arising from the coupling to the phonons, thus destroying the coherence which is essential for AB interferometry, as discussed below. This important result emphasizes yet another major difference between electric and magnetic gauges.

5.1. Hamiltonian

We consider a tight binding model of an atomic-corral-based interferometer. We describe the case of a single valence electron per atomic site where the interaction between the electrons and the vibrations occurs on site, namely an electron located at site i will couple to the local vibration of the ith atom. The Hamiltonian of the system is described by

$$\hat{H} = \hat{H}_{\rm el} + \hat{H}_{\rm vib} + \hat{H}_{\rm int}, \tag{44}$$

where $\hat{H}_{\rm el}$ is the electronic part of the Hamiltonian, $\hat{H}_{\rm vib}$ is the part of the Hamiltonian describing the vibrational modes of the molecule and $\hat{H}_{\rm int}$ represents the interaction of the electrons with the vibrations of the molecule.

The electronic part of the Hamiltonian may be written as a combination of two terms: $\hat{H}_{\rm el} = \hat{H}^0_{\rm el} + \hat{H}^{\rm int}_{\rm el}$, where $\hat{H}^0_{\rm el} = \hat{H}^{\rm device}_{\rm el} + \hat{H}^{\rm leads}_{\rm el}$, $\hat{H}^{\rm device}_{\rm el}$ being the electronic Hamiltonian of the isolated corral (or any other device), $\hat{H}^{\rm leads}_{\rm el}$ the electronic Hamiltonian of the bare leads and $\hat{H}^{\rm int}_{\rm el}$ is the lead–device electronic interaction Hamiltonian. One may write these terms using second quantization operators. For the non-interacting electronic Hamiltonian

$$\hat{H}^0_{\rm el} = \sum_{i,j} t_{i,j}(B) c_i^\dagger c_j + \sum_{l,m\in L,R} \epsilon_{l,m}(B) d_l^\dagger d_m, \tag{45}$$

where $c_i^\dagger$ and c_i, are creation and annihilation operators of an electron on site i on the device, and $d_l^\dagger$ and d_l are the creation and annihilation operators of an electron on site l on the relevant lead. $t_{i,j}(B)$ is the hopping integral between site i and site j on the device and $\epsilon_{l,m}(B)$ is the hopping integral between site l and site m on the relevant lead. As before, L and R stand for left and right leads.

For the device–lead interaction part

$$\hat{H}^{\rm int}_{\rm el} = \sum_{l,i} V_{l,i}(B) d_l^\dagger c_i + {\rm H.c.}, \tag{46}$$

where H.c. stands for Hermitian conjugate. The matrix elements of all these terms are evaluated using the TB-MEHT approach presented in section 4.4. Thus, $t_{i,j}(B)$, $\epsilon_{l,m}(B)$ and $V_{l,i}(B)$ depend on the magnetic field B.

When considering the vibrational part of the Hamiltonian, $\hat{H}_{\rm vib}$, the device atoms are allowed to vibrate around their equilibrium position such that one can describe their vibrations using the harmonic approximation. For the sake of simplicity the atoms are assumed to be confined to move along the circumference such that one can map the problem onto a one-dimensional (1D) chain of coupled harmonic oscillators with periodic boundary conditions. For the case of a corral composed of identical atoms, one has to define only the local vibrational frequency Ω in order to obtain all normal vibrations of the ring. In local modes, the vibrational Hamiltonian of the system is described by a simple form given by

$$H_{\rm vib} = T_{\rm vib} + V_{\rm vib} = \sum_{k=0}^{N-1} \frac{p_k^2}{2} + \frac{1}{2}\Omega^2 \sum_{k=0}^{N-1} (x_{k+1} - x_k)^2. \tag{47}$$

Here, N is the number of atoms, and p_k and x_k denote the mass-weighted momentum operator and the mass-weighted deviation from the equilibrium position of atom k along the chain, respectively. Periodic boundary conditions are imposed on the system such that $x_N = x_0$. It is possible to define a unitary transformation (given by a matrix $\hat{U}$) that diagonalizes the Hamiltonian (cf equation (47)) to obtain

$$H_{\rm vib} = T_{\rm vib} + V_{\rm vib} = \tfrac{1}{2} \sum_{k=0}^{N-1} {p_k^{(q)}}^2 + \tfrac{1}{2} \sum_{k=0}^{N-1} \omega_k^2 q_k^2, \tag{48}$$

This Hamiltonian represents a set of N uncoupled harmonic oscillators, each with frequency ω_k, of the collective normal mode of vibration q_k, where all frequencies are defined in terms of Ω and the unitary transformation $\hat{U}$. In terms of raising and lowering boson operators one finally arrives at

$$\hat{H}_{\rm vib} = \sum_{k=0}^{N-1} \hbar\omega_k \left(b_k^\dagger b_k + \tfrac{1}{2} \right). \tag{49}$$

The last term in the full Hamiltonian (equation (44)) is the electron–vibration coupling term. To lowest order in the electron–phonon coupling, this term is modeled by

$$\hat{H}_{\rm int} = M \sum_{i=0}^{N-1} c_i^\dagger c_i (a_i^\dagger + a_i). \tag{50}$$

where M is the electron–phonon coupling strength, which is taken to be identical to all atomic sites. Using this form, the electron on site i, represented by the number operator $N_i \equiv c_i^\dagger c_i$, is coupled to the local vibration of atom i, represented by $a_i^\dagger + a_i$. Here $a_i^\dagger$ and a_i are the raising and lowering operators of the local vibrational modes defined in terms of x_k and p_k such that $(a_k^\dagger + a_k) = \sqrt{\frac{2\Omega}{\hbar}}\hat{x}_k$. In terms of the normal modes of the ring, the electron–phonon coupling Hamiltonian is given by

$$\hat{H}_{\rm int} = M \sum_{i=0}^{N-1} c_i^\dagger c_i (a_i^\dagger + a_i) = \sum_{i,k=0}^{N-1} M_i^k c_i^\dagger c_i (b_k^\dagger + b_k), \tag{51}$$

where $M_i^k \equiv M\sqrt{\frac{\Omega}{\omega_k}} U_{ki}$ and U_{ki} are the matrix elements of the transformation matrix $\hat{U}$.

Collecting all the terms appearing in equations (45), (46), (49) and (51), the full Hamiltonian of the system is given by the following expression:

$$\hat{H} = \sum_{i,j} t_{i,j}(B) c_i^\dagger c_j + \sum_{l,m\in L,R} \epsilon_{l,m}(B) d_l^\dagger d_m + \left(\sum_{l,i} V_{l,i}(B) d_l^\dagger c_i + \text{H.c.} \right) + \sum_{k=0}^{N-1} \hbar\omega_k \left(b_k^\dagger b_k + \tfrac{1}{2} \right) + \sum_{i,k=0}^{N-1} M_i^k c_i^\dagger c_i (b_k^\dagger + b_k). \quad (52)$$

As pointed out above, the only two free parameters in this model are M—the electron–phonon coupling strength—and Ω—the local vibrational frequency. The remaining hopping terms are calculated from the TB-MEHT.

5.2. Conductance

The calculation of the conductance is described, as before, within the framework of the nonequilibrium Green's function (NEGF) method [119]. In brief, the total current $I = I_{\text{el}} + I_{\text{inel}}$ is recast as a sum of elastic (I_{el}) and inelastic (I_{inel}) contributions given by [165]

$$I_{\text{el}} = \frac{2e}{\hbar} \int \frac{\mathrm{d}\epsilon}{2\pi} \left[f(\epsilon, \mu_{\text{R}}) - f(\epsilon, \mu_{\text{L}}) \right] \times \text{Tr} \left[\mathbf{\Gamma}_{\text{L}}(\epsilon) \mathbf{G}^{\text{r}}(\epsilon) \mathbf{\Gamma}_{\text{R}}(\epsilon) \mathbf{G}^{\text{a}}(\epsilon) \right] \quad (53)$$

and

$$I_{\text{inel}} = \frac{2e}{\hbar} \int \frac{\mathrm{d}\epsilon}{2\pi} \text{Tr} \left[\mathbf{\Sigma}_{\text{L}}^{<}(\epsilon) \mathbf{G}^{\text{r}}(\epsilon) \mathbf{\Sigma}_{\text{ph}}^{>}(\epsilon) \mathbf{G}^{\text{a}}(\epsilon) - \mathbf{\Sigma}_{\text{L}}^{>}(\epsilon) \mathbf{G}^{\text{r}}(\epsilon) \mathbf{\Sigma}_{\text{ph}}^{<}(\epsilon) \mathbf{G}^{\text{a}}(\epsilon) \right], \quad (54)$$

respectively. The retarded (advanced) GFs satisfy the Dyson equation:

$$\mathbf{G}^{\text{r,a}}(\epsilon) = \left\{ [\mathbf{g}^{\text{r,a}}(\epsilon)]^{-1} - \mathbf{\Sigma}_{\text{L}}^{\text{r,a}}(\epsilon) - \mathbf{\Sigma}_{\text{R}}^{\text{r,a}}(\epsilon) - \mathbf{\Sigma}_{\text{ph}}^{\text{r,a}}(\epsilon) \right\}^{-1}, \quad (55)$$

where $\mathbf{g}^{\text{r,a}}(\epsilon)$ is the uncoupled retarded (advanced) electronic GF of the ring. In the above equations, the retarded (advanced) self-energy arising from the coupling to the right (left) lead is $\mathbf{\Sigma}_{\text{L,R}}^{\text{r,a}}(\epsilon) = (\epsilon - \mathbf{V}^\dagger(B)) \mathbf{g}_{\text{L,R}}^{\text{r,a}}(\epsilon) (\epsilon - \mathbf{V}(B))$, the corresponding greater (lesser) self-energy is $\mathbf{\Sigma}_{\text{L,R}}^{\lessgtr}(\epsilon) = (\delta_{\lessgtr} - f(\epsilon, \mu_{\text{L,R}}))[\mathbf{\Sigma}_{\text{L,R}}^{\text{r}}(\epsilon) - \mathbf{\Sigma}_{\text{L,R}}^{\text{a}}(\epsilon)]$, where $\delta_{\lessgtr}$ equals 0 for $<$ and 1 otherwise, $f(\epsilon, \mu) = \frac{1}{1+e^{\beta(\epsilon-\mu)}}$ and $\mathbf{\Gamma}_{\text{L,R}}(\epsilon) = \text{i}[\mathbf{\Sigma}_{\text{L,R}}^{\text{r}}(\epsilon) - \mathbf{\Sigma}_{\text{L,R}}^{\text{a}}(\epsilon)]$. To obtain these self-energies one requires as input the lead–ring hopping matrix $\mathbf{V}(B)$ with elements $V_{mj}(B)$ and the retarded (advanced) uncoupled GF of the left or right lead $\mathbf{g}_{\text{L,R}}^{\text{r,a}}(\epsilon)$. The calculation of the current requires also the self-energy arising from the interactions with the phonons, which in the present study is calculated using the first Born approximation (FBA), and is given by [165]

$$\mathbf{\Sigma}_{\text{ph}}^{\text{r}}(\epsilon) = \text{i} \sum_k \int \frac{\mathrm{d}\omega}{2\pi} \mathbf{M}^k \left\{ D_k^{<}(\omega) \mathbf{g}^{\text{r}}(\epsilon - \omega) + D_k^{\text{r}}(\omega) \mathbf{g}^{<}(\epsilon - \omega) + D_k^{\text{r}}(\omega) \mathbf{g}^{\text{r}}(\epsilon - \omega) \right\} \mathbf{M}^k, \quad (56)$$

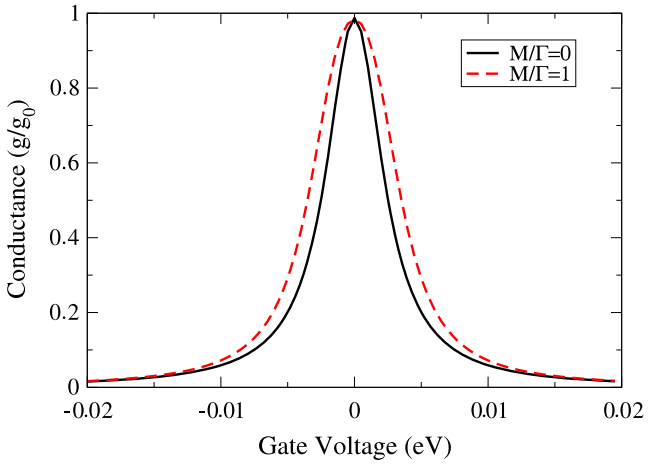

Figure 24. Conductance versus gate voltage for a single energy level coupled to two electronic reservoirs in the absence (solid line) and the presence (dashed line) of an interaction with a single vibrational mode.

where the Hartree term has been omitted [244]. The lesser and greater self-energies arising from the coupling to the phonons are given by

$$\mathbf{\Sigma}_{\text{ph}}^{\lessgtr}(\epsilon) = \text{i} \sum_k \int \frac{\mathrm{d}\omega}{2\pi} \mathbf{M}^k D_k^{\lessgtr}(\omega) \mathbf{g}^{\lessgtr}(\epsilon - \omega) \mathbf{M}^k. \quad (57)$$

In the above equations, $D_k^{\text{r,a}}$ and $D_k^{\lessgtr}$ are the uncoupled equilibrium retarded (advanced) and lesser (greater) GFs of phonon mode k, respectively, $\mathbf{g}^{\lessgtr}(\epsilon)$ is the lesser (greater) uncoupled electronic GF of the ring and $\mathbf{M}^k$ is the EPC matrix of mode k (diagonal in the c_j basis).

One should keep in mind that the first Born approximation is a truncation of the self-consistent Born procedure which by itself is an approximation to the solution of the real many-body problem. Therefore, only the low electron–phonon coupling regime can be considered within the framework of this model [244, 156].

5.3. Results

First, we discuss the influence of electron–vibration coupling on the gate voltage dependence of the zero bias, zero temperature conductance in the absence of a magnetic field. For simplicity we start by considering a single energy level coupled to a single vibrational mode. The results are shown in figure 24. The vibrational frequency, Ω, is taken to give $\hbar\Omega = 0.01$ eV, the coupling to the leads is considered to be symmetric such that $\Gamma_{\text{L}} = \Gamma_{\text{R}} = 0.25\hbar\Omega$ and $\Gamma = \Gamma_{\text{L}} + \Gamma_{\text{R}} = 0.5\hbar\omega_0$, and the width of the vibrational energy levels due to their relaxation to an external thermal bath is taken as $\eta = 2 \times 10^{-4}$ eV. We plot the conductance as a function of the gate potential for the case of no vibrational coupling ($\frac{M}{\Gamma} = 0$) and for the case where the coupling of the electron to the nuclear vibrations of the device equals the coupling of the device to the leads ($\frac{M}{\Gamma} = 1$), where M is the coupling strength to the vibrational mode. The latter condition defines the upper

limit for the relevance of the perturbative treatment discussed in the last section [244].

The two most significant observations are the expected broadening of the conduction when the EPC is turned on and the value of the zero bias conduction ($g/g_0 = 1$, where $g_0 = 2e^2/h$ is the quantum conductance) in the presence of EPC. To better understand these results we rewrite the current for the case that $\mathbf{\Gamma}_L(\epsilon) = \mathbf{\Gamma}_R(\epsilon) \equiv \mathbf{\Gamma}(\epsilon)/2$ in the following way [251]: $I = \frac{2e}{h}\int d\epsilon (f(\epsilon-\mu_L) - f(\epsilon-\mu_R))\mathcal{T}(\epsilon)$, where $\mathcal{T}(\epsilon) = \frac{i}{4}\mathrm{Tr}\,\mathbf{\Gamma}(\epsilon)(\mathbf{G}^r(\epsilon) - \mathbf{G}^a(\epsilon))$. Note that $\mathcal{T}(\epsilon)$ is the transmission coefficient only when $M = 0$. In the wide band limit, for the single resonant level model, $\mathcal{T}(\epsilon)$ can be reduced to $\frac{\Gamma}{4}\frac{\Gamma - 2\Sigma^r_{ph,im}(\epsilon)}{(\epsilon-\epsilon_0-\Sigma^r_{ph,re}(\epsilon))^2+(\Gamma/2-\Sigma^r_{ph,im}(\epsilon))^2}$. As a result of the fact that $\Sigma^r_{ph,im}(0) = 0$ at zero bias, the only inelastic contribution to the conduction comes from the real part of the phonon self-energy [244]. From this, it follows that, even in the presence of EPC, the maximal conduction is $g_{max}/g_0 = 1$, as can clearly be seen in figure 24. It also immediately implies that the main contribution to the broadening of the resonant conduction peak comes from the energy-dependent real part of the phonon self-energy.

Next, we consider a similar situation in a molecular AB interferometer composed of $N = 40$ sites. The sites are identical and contribute a single electron which is described by a single Slater s-like orbital. The coupling between the ring and the leads is limited to the contact region. For simplicity, the electronic self-energies arising from this coupling are approximated within the wide band limit. Specifically, we approximate $\mathbf{\Gamma}_{L,R}(\epsilon)$ with matrices that are independent of energy, where the only non-vanishing elements are the diagonal elements ($\Gamma_{L,R}$) corresponding to the two sites coupled to the left or right lead. The local phonon frequency $\Omega = 0.0125$ eV is characteristic of a low frequency optical phonon in molecular devices [252, 253]. Since our model does not include a secondary phonon bath required to relax the energy from the optical phonons, we include a phonon energy level broadening $\eta = 0.016\ \Omega$. The coupling to each of the leads is taken to be $\Gamma_L = \Gamma_R = 4\ \Omega$ such that the magnetoconductance switching in the absence of EPC is obtained at ∼5 T for an inter-site separation of $\frac{1.5}{\xi}$, where ξ is the inverse correlation length of the Slater s-like orbital ($\xi = 1.3$ in atomic units).

In figure 25 a similar plot is presented for the two degenerate levels of the atomic corral. As can be seen, the picture that arises in the corral case (figure 25) resembles that obtained for a single level (figure 24). The difference in the width of the lineshapes between the two cases results from the fact that the coupling to the electronic reservoirs is different and that the coupling strength of the molecular levels to the vibrations in the corral case is not given by M itself but by a set of transformations proportional to M, as described in section 5.1.

We now turn to discuss the role of EPC on the magnetoconduction when the gate voltage is fixed to zero, such that at zero magnetic field the corral fully conducts. In figure 26 we plot the magnetoconductance of the AB ring for several values of the EPC (M) and for different temperatures (T). We focus on the regime of low magnetic flux $\phi = AB$,

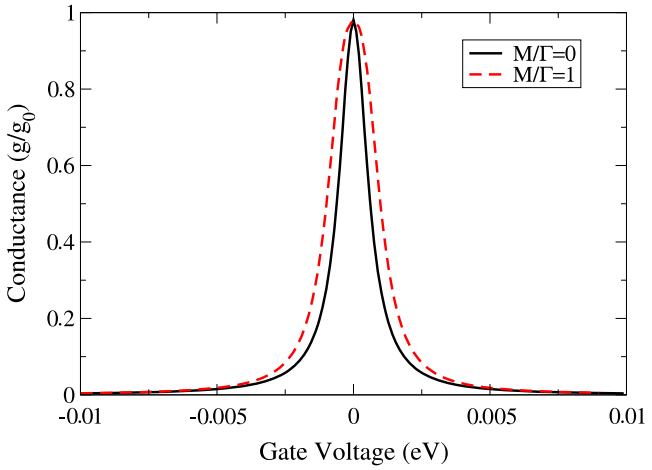

Figure 25. Conductance versus gate voltage for a 40-site atomic corral coupled to two electronic reservoirs in the absence (solid line) and the presence (dashed line) of electron–vibration interactions.

where A is the area of the ring and B is taken perpendicular to the plane of the ring.

The case $M = 0$ was discussed in detail in sections 3 and 4. The solid curves in figure 26 present the coherent magnetoconductance switching for different temperatures. As expected, we find that, upon increasing the temperature, the maximal value of g/g_0 is decreased and the width of the magnetoconductance peaks is increased linearly with T. This increase in the width with temperature is a result of the resonant tunneling conditions and the broadening of the leads' Fermi distribution functions as T is varied.

Turning to discuss the case of $M \neq 0$, one of the major questions is related to the effects of EPC on the switching capability of small AB rings. Based on the discussion of the results when the gate voltage was varied, one might expect that an increase in M will lead to a broadening of the magnetoconductance peaks, thereby increasing the value of the magnetic field required to switch a nanometer AB ring, and perhaps leads to unphysical values of B required to reduced the conduction significantly. As can be seen in figure 26, the numerical solution of the NEGF for $M \neq 0$ leads to a *reduction* of the width of the magnetoconductance peaks, and the switching of the AB ring is achieved at lower values of the magnetic flux compared to the case where $M = 0$.

This surprising observation can be explained in simple terms [114]. As discussed above, even in the presence of EPC, the maximal conduction at zero bias and zero temperature is $g_{max}/g_0 = 1$, as is clearly the case for the results shown in the upper left panel of figure 26 for $\phi/\phi_0 = 0$. For the symmetric ring of $N = 4n$ the resonance condition at $\phi/\phi_0 = 0$ is equivalent to the condition that electrons entering the ring from the left *interfere constructively* when they exit the ring to the right [254, 255]. This picture also holds when $M \neq 0$ and the conduction takes a maximal value at $\phi/\phi_0 = 0$. The application of a magnetic field leads to destructive interference and increases the backscattering of electrons. This loss of phase is even more pronounced when inelastic effects arising from EPC are included. In the magnetoconductance this is

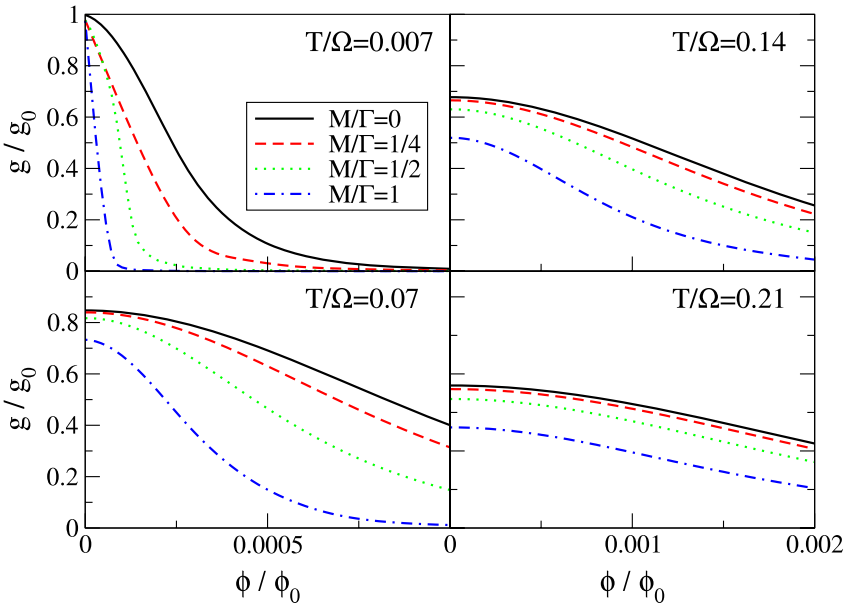

Figure 26. Conductance as a function of magnetic flux for several values of the EPC strength M and for different temperatures. The results are for a ring of $N = 40$ sites. Similar results were obtained for larger/smaller rings, signifying that the scaling behavior [254, 255] for the phonon-free case also holds in the case of weak EPC.

translated to a more rapid loss of conduction as a function of the magnetic field when M is increased. In the weak device–lead coupling limit, the same physics also describes other classes of rings [254, 255], like the $N = 4n + 1$, $N = 4n + 2$ and $N = 4n + 3$. However, a gate voltage must be applied to tune the resonance such that conduction is maximal at zero magnetic field [111].

Mathematically, the rapid decay of the conduction with the magnetic field as the EPC is increased can be explained by analyzing the dependence of $\mathcal{T}(\epsilon)$. In figure 27 we plot $\mathcal{T}_{\rm el}(\epsilon) = {\rm Tr}[\mathbf{\Gamma}_{\rm L}(\epsilon)\mathbf{G}^{\rm r}(\epsilon)\mathbf{\Gamma}_{\rm R}(\epsilon)\mathbf{G}^{\rm a}(\epsilon)]$, which is the elastic (and dominant) contribution to $\mathcal{T}(\epsilon)$ as a function of energy for several values of ϕ/ϕ_0 for $M/\Gamma = 0$ or $M/\Gamma = \frac{1}{4}$. In the lower panel we also plot the corresponding Fermi distribution integration window. At $\phi/\phi_0 = 0$, $\mathcal{T}_{\rm el}(\epsilon) \approx 1$ near the Fermi energy ($\epsilon_{\rm f}$), independent of M, and the conduction is $g/g_0 \approx 1$. The application of a small magnetic field results in a split of $\mathcal{T}_{\rm el}(\epsilon)$, where each peak corresponds to a different circular state [256]. The separation between the two peaks in the elastic limit $\Delta = (\epsilon_2 - \epsilon_1) \propto \phi/\phi_0$ is proportional to the magnetic flux, where $\epsilon_{1,2}$ are the corresponding energies of the two circular states. When inelastic terms are included, due to the fact that the imaginary part of $\mathbf{\Sigma}^{\rm r}_{\rm ph}(\epsilon)$ is negligibly small, the renormalized positions of the two peaks can be approximated by $\epsilon^*_{1,2} = \epsilon_{1,2} + \Sigma^{\rm r}_{\rm ph,re}(\epsilon_{1,2}) = \epsilon_{1,2} \pm \Sigma^{\rm r}_{\rm ph,re}(\epsilon_2)$, which implies that the renormalized separation between the two peaks can be approximated by $\Delta^* = (\epsilon^*_2 - \epsilon^*_1) = \Delta + 2\Sigma^{\rm r}_{\rm ph,re}(\epsilon_2)$. Therefore, as M is increased Δ^* is also increased, consistent with the numerical results shown in figure 27.

To summarize this section, as expected, the gate voltage dependence of the conductance broadens upon switching on the electron–vibration coupling. Nevertheless, the magnetoconductance peaks reduce both in size and in width when the vibrational coupling is taken into account. This implies a higher sensitivity of the device to the application of an external magnetic field than that predicted for the pure coherent case.

6. Summary and prospects

Affecting the current through molecular or nanoscale junctions is usually done by a combination of bias and gate voltages. Magnetic fields are less studied because nanodevices can capture only small fractions of a magnetic flux. In particular, exploiting Aharonov–Bohm interferometers at the nanometer scale was regarded as impossible due to the large magnetic field required to complete a full Aharonov–Bohm period.

The present review summarizes an attempt to overcome some of the limitations associated with utilizing magnetic fields as gates in molecular junctions. We describe the physical conditions at which magnetic fields significantly affect the conductance in molecular Aharonov–Bohm interferometers. Several examples were given to emphasize the major differences between electric and magnetic gates.

Using a simple continuum model of an Aharonov–Bohm interferometer ring that captures the essential physical features of the problem, we have identified and isolated the important parameters that allow control over the conductance through a nanometric ring using fractions of a magnetic flux (in terms of the quantum flux). In contrast to the strive to gain better coupling between the leads and the molecule within a molecular junction, magnetic control requires weak device–lead couplings (bad contacts). This results in a resonant tunneling junction in which the weakly coupled (and thus extremely narrow) energy levels of the ring allow the transport only at well-defined energy values. By the application of a gate voltage it is possible to tune these resonances such that, in the absence of a magnetic field, the device will conduct. Turning

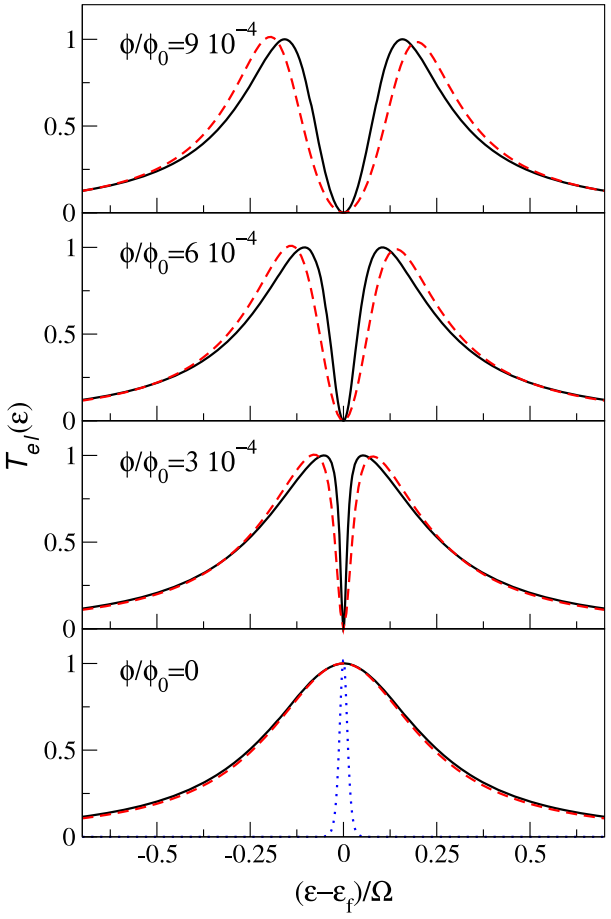

Figure 27. Plots of $\mathcal{T}_{\rm el}(\epsilon)$ as a function of energy for $M/\Gamma = 0$ (solid curves) and $M/\Gamma = \frac{1}{4}$ (dashed curves) for different values of the magnetic flux. The dotted curve at the lower panel shows $\frac{\partial}{\partial\mu}\Delta f(\epsilon-\mu)$ at $T/\Omega = 0.007$, where $\Delta f(\epsilon-\mu)$ is the difference between the Fermi distributions of the left and right leads.

on a magnetic field will shift the narrow doubly degenerate energy levels of the ring out of resonance with the leads and thus will lower the conductance considerably. Considering the combined effect of increasing the lifetime of the electron on the ring (through the coupling) and controlling its energy (using a gate voltage), it is possible to narrow the magnetoconductance peaks in the Aharonov–Bohm spectrum while at the same time shifting them toward the low magnetic field regime, such that the device becomes extremely sensitive to small magnetic fields. This is despite the fact that the full Aharonov–Bohm period involves magnetic fields orders of magnitude higher.

In order to validate the basic principles revealed by the continuum model we have presented results based on a tight binding magnetic extended Hückel theory, which allows for atomistic calculation of the conductance through molecular set-ups under the influence of an external magnetic field. Similar to the conclusions drawn from the continuum model, the results obtained from atomistic calculation indicate that nanometric circular set-ups such as atomic corrals, the cross section of carbon nanotubes or polycyclic aromatic rings, can be used for Aharonov–Bohm interferometry. The conductance through the device becomes very sensitive to the magnetic field when a delicate balance of coupling and gate/bias voltages is reached. Such devices can be used as electromagnetic switches or as miniature magnetic sensors.

Similar to the electric gate, the magnetic field provides means to externally control the conductance of ring-shaped molecular junctions. However, there are striking differences in the properties of these two gauges. This was illustrated in a multi-terminal device, where the polarity of the magnetic field, which couples to the electronic angular momentum, played a key role. In this device, the unique symmetry breaking nature of the magnetic vector potential allows for a selective control over the outgoing route of the electron. The magnetic field polarity determines through which of the two outgoing leads the electrons will transverse the ring. Another fundamental difference between electrical and magnetic gauges was observed with respect to inelastic effects. While the conductance as a function of the gate voltage broadens upon coupling to phonons, it actually narrows considerably in response to a magnetic field. This was illustrated for a model system of an atomic corral, where improved switching capability was observed as the electron–phonon coupling strength was increased.

The design of molecular junctions is an extremely difficult task. Moreover, introducing external electrical gates is quite limited and the fabrication and application of gate electrodes at the nanometer scale is still not feasible. In this context, the development of molecular Aharonov–Bohm interferometers sensitive to uniform magnetic fields provides yet another advantage over electrical gating. Devices can be designed utilizing different sizes/shapes of rings that function at different magnetic fields, thus generating a multi-component structure.

Several issues still remain open. Most importantly is the experimental realization of the proposed theoretical scheme. We have suggested several realistic systems where the effects discussed in this review can be measured. On the theoretical side, several directions are not covered here. First, a treatment of high electron–phonon coupling is needed [247]. In this regime it is reasonable to expect that the coherent nature of the transport would be destroyed, diminishing the interference pattern. Therefore, it is important to identify the physical conditions at which such effects are expected to be found. Furthermore, the treatment of strongly correlated systems where electron–electron interactions become important is also an open subject not addressed in the context of molecular Aharonov–Bohm interferometers. Another interesting direction involves the role of the spin of the current carrying particles. Since opposite spins respond differently when entering a magnetic field region, one would expect that their Aharonov–Bohm interference patterns would be different [145]. Thus, such set-ups can provide the grounds for the development of spintronic devices based on molecular Aharonov–Bohm interferometers.

References

[1] Jortner J and Ratner M 1997 *Molecular Electronics* (New York: Blackwell Science)
[2] Roth C and Joachim C 1997 *Atomic and Molecular Wires* (Dordrecht: Kluwer)

[3] Emberly E G and Kirczenow G 1998 Theory of electrical conduction through a molecule *Mol. Electron. Sci. Technol.* **852** 54–67

[4] Dekker C 1999 Carbon nanotubes as molecular quantum wires *Phys. Today* **52** 22–8

[5] Ratner M 2000 Molecular electronics—pushing electrons around *Nature* **404** 137–8

[6] Joachim C, Gimzewski J K and Aviram A 2000 Electronics using hybrid-molecular and mono-molecular devices *Nature* **408** 541–8

[7] Tour J M 2000 Molecular electronics. synthesis and testing of components *Acc. Chem. Res.* **33** 791–804

[8] Nitzan A 2001 Electron transmission through molecules and molecular interfaces *Annu. Rev. Phys. Chem.* **52** 681–750

[9] Pantelides S T, Di Ventra M and Lang N D 2001 Molecular electronics by the numbers *Physica* B **296** 72–7

[10] Bourgoin J-P 2001 Molecular electronics: a review of metal–molecule–metal junctions *Lect. Notes Phys.* **579** 105

[11] Avouris P 2002 Molecular electronics with carbon nanotubes *Acc. Chem. Res.* **35** 1026–34

[12] Nitzan A and Ratner M A 2003 Electron transport in molecular wire junctions *Science* **300** 1384–9

[13] Heath J R and Ratner M A 2003 Molecular electronic *Phys. Today* **56** 43–9

[14] Hush N S 2003 An overview of the first half-century of molecular electronics *Ann. New York Acad. Sci.* **1006** 1–20

[15] Wassel R A and Gorman C B 2004 Establishing the molecular basis for molecular electronics *Angew. Chem. Int. Edn Engl.* **43** 5120–3

[16] Seminario J M 2005 Molecular electronics: approaching reality *Nat. Mater.* **4** 111–3

[17] Joachim C and Ratner M A 2005 Molecular electronics: some views on transport junctions and beyond *Proc. Natl Acad. Sci.* **102** 8801–8

[18] Tao N J 2006 Electron transport in molecular junctions *Nat. Nanotechnol.* **1** 173–81

[19] Prasanna de Silva A and Uchiyama S 2007 Molecular logic and computing *Nat. Nanotechnol.* **2** 399–10

[20] Park H 2007 Molecular electronics: charges feel the heat *Nat. Mater.* **6** 330–1

[21] Reddy P, Jang S-Y, Segalman R A and Majumdar A 2007 Thermoelectricity in molecular junctions *Science* **315** 1568–71

[22] Weibel N, Grunder S and Mayor M 2007 Functional molecules in electronic circuits *Org. Biomol. Chem.* **5** 2343–53

[23] Franzon P, Nackashi D, Amsinck C, DiSpigna N and Sonkusale S 2007 Molecular electronics—devices and circuits technology *IFIP Int. Federation Inf. Process.* **240** 1–10

[24] Aviram A and Ratner M A 1974 Molecular rectifiers *Chem. Phys. Lett.* **29** 277

[25] Reed M A, Zhou C, Muller C J, Burgin T P and Tour J M 1997 Conductance of a molecular junction *Science* **278** 252–4

[26] Kergueris C, Bourgoin J P, Palacin S, Esteve D, Urbina C, Magoga M and Joachim C 1999 Electron transport through a metal–molecule–metal junction *Phys. Rev. B* **59** 12505–13

[27] Weber H B, Reichert J, Weigend F, Ochs R, Beckmann D, Mayor M, Ahlrichs R and von Lohneysen H 2002 Electronic transport through single conjugated molecules *Chem. Phys.* **281** 113–25

[28] Smit R H M, Noat Y, Untiedt C, Lang N D, van Hemert M C and van Ruitenbeek J M 2002 Measurement of the conductance of a hydrogen molecule *Nature* **419** 906–9

[29] Park H, Lim A K L, Alivisatos A P, Park J and McEuen P L 1999 Fabrication of metallic electrodes with nanometer separation by electromigration *Appl. Phys. Lett.* **75** 301–3

[30] Liang W J, Shores M P, Bockrath M, Long J R and Park H 2002 Kondo resonance in a single-molecule transistor *Nature* **417** 725

[31] Selzer Y, Cai L T, Cabassi M A, Yao Y X, Tour J M, Mayer T S and Allara D L 2005 Effect of local environment on molecular conduction: isolated molecule versus self-assembled monolayer *Nano Lett.* **5** 61–5

[32] Selzer Y and Allara D L 2006 Single-molecule electrical junctions *Annu. Rev. Phys. Chem.* **57** 593–623

[33] Guillorn M A, Carr D W, Tiberio R C, Greenbaum E and Simpson M L 2000 Fabrication of dissimilar metal electrodes with nanometer interelectrode distance for molecular electronic device characterization *J. Vac. Sci. Technol.* B **18** 1177–81

[34] Park J *et al* 2002 Coulomb blockade and the Kondo effect in single atom transistors *Nature* **417** 722–5

[35] Hersam M C, Guisinger N P and Lyding J W 2000 Silicon-based molecular nanotechnology *Nanotechnology* **11** 70–6

[36] Klein D L, McEuen P L, Bowen Katari J E, Roth R and Alivisatos A P 1996 An approach to electrical studies of single nanocrystals *Appl. Phys. Lett.* **68** 2574–6

[37] Davidovic D and Tinkham M 1998 Coulomb blockade and discrete energy levels in Au nanoparticles *Appl. Phys. Lett.* **73** 3959–61

[38] Morpurgo A F, Marcus C M and Robinson D B 1999 Controlled fabrication of metallic electrodes with atomic separation *Appl. Phys. Lett.* **74** 2084–6

[39] Li C Z, He H X and Tao N J 2000 Quantized tunneling current in the metallic N formed by electrodeposition and etching *Appl. Phys. Lett.* **77** 3995–7

[40] Kervennic Y V, Van der Zant H S J, Morpurgo A F, Gurevich L and Kouwenhoven L P 2002 Nanometer-spaced electrodes with calibrated separation *Appl. Phys. Lett.* **80** 321–3

[41] Frank S, Poncharal P, Wang Z L and de Heer W A 1998 Carbon nanotube quantum resistors *Science* **280** 1744 ett

[42] Slowinski K, Fong H K Y and Majda M 1999 Mercury–mercury tunneling junctions. 1. Electron tunneling across symmetric and asymmetric alkanethiolate bilayers *J. Am. Chem. Soc.* **121** 7257–61

[43] Holmlin R E, Haag R, Chabinyc M L, Ismagilov R F, Cohen A E, Terfort A, Rampi M A and Whitesides G M 2001 Electron transport through thin organic films in metal–insulator–metal junctions based on self-assembled monolayers *J. Am. Chem. Soc.* **123** 5075–85

[44] Kushmerick J G, Holt D B, Yang J C, Naciri J, Moore M H and Shashidhar R 2002 Metal–molecule contacts and charge transport across monomolecular layers: measurement and theory *Phys. Rev. Lett.* **89** 086802

[45] Dorogi M, Gomez J, Osifchin R, Andres R P and Reifenberger R 1995 Room-temperature Coulomb blockade from a self-assembled molecular nanostructure *Phys. Rev.* B **52** 9071–7

[46] Gittins D I, Bethell D, Schiffrin D J and Nichol R J 2000 A nanometre-scale electronic switch consisting of a metal cluster and redox-addressable groups *Nature* **408** 67

[47] Cui X D, Primak A, Zarate X, Tomfohr J, Sankey O F, Moore A L, Moore T A, Gust D, Harris G and Lindsay S M 2001 Reproducible measurement of single-molecule conductivity *Science* **294** 571–4

[48] Tans S J, Devoret M H, Dai H, Thess A, Smalley R E, Geerligs L J and Dekker C 1997 Individual single-wall carbon nanotubes as quantum wires *Nature* **386** 474

[49] Porath D, Bezryadin A, de Vries S and Dekker C 2000 Direct measurement of electrical transport through DNA molecules *Nature* **403** 635–8

[50] Dadoshand T, Gordin Y, Krahne R, Khivrich I, Mahalu D, Frydman V, Sperling J, Yacoby A and Bar-Joseph I 2005

Measurement of the conductance of single conjugated molecules *Nature* **436** 677–80
[51] Klein D L, Roth R, Lim A K L, Alivisatos A P and McEuen P L 1997 A single-electron transistor made from a cadmium selenide nanocrystal *Nature* **389** 699–701
[52] Tans S J, Verschueren A R M and Dekker C 1998 Room-temperature transistor based on a single carbon nanotube *Nature* **393** 49–52
[53] Yao Z, Postma H W Ch, Balents L and Dekker C 1999 Carbon nanotube intramolecular junctions *Nature* **402** 273
[54] Chen J, Reed M A, Rawlett A M and Tour J M 1999 Large on–off ratios and negative differential resistance in a molecular electronic device *Science* **286** 1550–2
[55] Postma H W Ch, Teepen T, Yao Z, Grifoni M and Dekker C 2001 Carbon nanotube single-electron transistors at room temperature *Science* **293** 76
[56] Cui Y and Lieber C M 2001 Functional nanoscale electronic devices assembled using silicon nanowire building blocks *Science* **291** 851–3
[57] Zhitenev N B, Meng H and Bao Z 2002 Conductance of small molecular junctions *Phys. Rev. Lett.* **88** 226801
[58] Luo Y *et al* 2002 Two-dimensional molecular electronics circuits *ChemPhysChem* **3** 519–25
[59] Liang W, Shores M P, Bockrath M, Long J R and Park H 2002 Kondo resonance in a single-molecule transistor *Nature* **417** 725–9
[60] Keren K, Berman R S, Buchstab E, Sivan U and Braun E 2003 DNA-templated carbon nanotube field-effect transistor *Science* **302** 1380–2
[61] Novoselov K S, Geim A K, Morozov S V, Jiang D, Zhang Y, Dubonos S V, Grigorieva I V and Firsov A A 2004 Electric field effect in atomically thin carbon films *Science* **306** 666–9
[62] Piva P G, DiLabio G A, Pitters J L, Zikovsky J, Rezeq M, Dogel S, Hofer W A and Wolkow R A 2005 Field regulation of single-molecule conductivity by a charged surface atom *Nature* **435** 658–61
[63] Champagne A R, Pasupathy A N and Ralph D C 2005 Mechanically adjustable and electrically gated single-molecule transistors *Nano Lett.* **5** 305–8
[64] Novoselov K S, Geim A K, Morozov S V, Jiang D, Katsnelson M I, Grigorieva I V, Dubonos S V and Firsov A A 2005 Two-dimensional gas of massless dirac fermions in graphene *Nature* **438** 197–200
[65] Li X, Xu B, Xiao X, Yang X, Zang L and Tao N 2006 Controlling charge transport in single molecules using electrochemical gate *Faraday Discuss.* **131** 111–20
[66] Berger C *et al* 2006 Electronic confinement and coherence in patterned epitaxial graphene *Science* **312** 1191–6
[67] Han M Y, Özyilmaz B, Zhang Y and Kim P 2007 Energy band-gap engineering of graphene nanoribbons *Phys. Rev. Lett.* **98** 206805
[68] Lemme M C, Echtermeyer T J, Baus M and Kurz H 2007 A graphene field effect device *IEEE Electron Device Lett.* **28** 282–4
[69] Klitzing K V, Dorda G and Pepper M 1980 New method for high-accuracy determination of the fine-structure constant based on quantized Hall resistance *Phys. Rev. Lett.* **45** 494–7
[70] Eherenberg W and Siday R E 1949 The refractive index in electron optics and the principles of dynamics *Proc. Phys. Soc. (London)* B **62** 8
[71] Aharonov Y and Bohm D 1959 Significance of electromagnetic potentials in the quantum theory *Phys. Rev.* **115** 485
[72] Chambers R G 1960 Shift of an electron interference pattern by enclosed magnetic flux *Phys. Rev. Lett.* **5** 3–5
[73] Parks R D and Little W A 1964 Fluxoid quantization in a multiply-connected superconductor *Phys. Rev.* **133** 000A97
[74] Sharvin D Yu and Sharvin Yu V 1981 Quantization of a magnetic flux in a cylindrical film from normal metal *JETP Lett.* **34** 272
[75] Al'tshuler B L, Aronov A G, Spivak B Z, Sharvin D Yu and Sharvin Yu V 1982 Observation of the Aharonov–Bohm effect in hollow metal cylinders *JETP Lett.* **35** 588–90
[76] Möllensdedt G, Schmid H and Lichte H 1982 *Proc. 10th Int. Congress on Electron Microscopy* (Hamburg: Deutschgesellschaft für Elektronen Mikroskopie)
[77] Tonomura A, Matsuda T, Suzuki R, Fukuhara A, Osakabe N, Umezaki H, Endo J, Shinagawa K, Sugita Y and Fujiwara H 1982 Observation of Aharonov–Bohm effect by electron holography *Phys. Rev. Lett.* **48** 1443–6
[78] Brandt N B, Bogachek E N, Gitsu D V, Gogadze G A, Kulik I O, Nikolaeva A A and Ponomarev Ya G 1982 Flux quantization effects in metallic microcylinders in tilted magnetic field *Fiz. Nisk. Temp.* **8** 718
[79] Ladan F R and Maurer J 1983 Magnetic flux quantization in a thin non-superconducting metal cylinder *C. R. Acad. Sci.* **297** 227–9
[80] Schmid H 1984 *Proc. 8th European Congress on Electron Microscopy* ed A Csanady, P Rohlich and D Szabo (Budapest: Programme Committee of the 8th Eur. Congr. on Electron Microsc.)
[81] Gijs M, van Haesandonck C and Bruynseraede Y 1984 Resistance oscillations and electron localization in cylindrical Mg films *Phys. Rev. Lett.* **52** 2069
[82] Gijs M, van Haesandonck C and Bruynseraede Y 1984 Quantum oscillations in the superconducting fluctuation regime of cylindrical Al films *Phys. Rev.* B **30** 2964–7
[83] Pannetier B, Chaussy J, Rammal R and Gandit P 1984 Magnetic flux quantization in the weak-localization regime of a nonsuperconducting metal *Phys. Rev. Lett.* **53** 718–21
[84] Sharvin Yu V 1984 Weak localization and oscillatory magnetoresistance of cylindrical metal films *Physica* B+C **126** 288–93
[85] Gordon J M 1984 Quantum phase sensitivity to macroscopic boundaries: Al cylinders and wires *Phys. Rev.* B **30** 6770–3
[86] Pannetier B, Chaussy J, Rammal R and Gandit P 1985 First observation of Altshuler–Aronov–Spivak effect in gold and copper *Phys. Rev.* B **31** 3209–11
[87] Dolan G J 1985 *Bull. Am. Phys. Soc.* **30** 395
[88] Al'tshuler B L, Aronov A G and Spivak B Z 1981 The Aharonov–Bohm effect in disordered conductors *JETP Lett.* **33** 94
[89] Büttiker M, Imry Y and Landauer R 1983 Josephson behavior in small normal one-dimensional rings *Phys. Lett.* A **96** 365
[90] Gefen Y, Imry Y and Azbel M Ya 1984 Quantum oscillations in small rings at low temperatures *Surf. Sci.* **142** 203
[91] Gefen Y, Imry Y and Azbel M Ya 1984 Quantum oscillations and the Aharonov–Bohm effect for parallel resistors *Phys. Rev. Lett.* **52** 129–32
[92] Büttiker M, Imry Y and Azbel M Ya 1984 Quantum oscillations in one-dimensional normal-metal rings *Phys. Rev.* A **30** 1982–9
[93] Carini J P, Muttalib K A and Nagel S R 1984 Origin of the Bohm–Aharonov effect with half flux quanta *Phys. Rev. Lett.* **53** 102–5
[94] Browne D A, Carini J P, Muttalib K A and Nagel S R 1984 Periodicity of transport coefficients with half flux quanta in the Aharonov–Bohm effect *Phys. Rev.* B **30** 6798–800
[95] Büttiker M, Imry Y, Landauer R and Pinhas S 1985 Generalized many-channel conductance formula with application to small rings *Phys. Rev.* B **31** 6207–15
[96] Webb R A, Washburn S, Umbach C P and Laibowitz R B 1985 Observation of h/e Aharonov–Bohm oscillations in normal-metal rings *Phys. Rev. Lett.* **54** 2696–9
[97] Timp G, Chang A M, Cunningham J E, Chang T Y, Mankiewich P, Behringer R and Howard R E 1987

Observation of the Aharonov–Bohm effect for $\omega_c\tau > 1$ *Phys. Rev. Lett.* **58** 2814–7
[98] Yacoby A, Heiblum M, Mahalu D and Shtrikman H 1995 Coherence and phase sensitive measurements in a quantum dot *Phys. Rev. Lett.* **74** 4047
[99] van Oudenaarden A, Devoret M H, Nazarov Yu V and Mooij J E 1998 Magneto-electric Aharonov–Bohm effect in metal rings *Nature* **391** 768–70
[100] Auslaender O M, Yacoby A, de Picciotto R, Baldwin K W, Pfeiffer L N and West K W 2002 Tunneling spectroscopy of the elementary excitations in a one-dimensional wire *Science* **295** 825–8
[101] Ralph D C, Black C T and Tinkham M 1997 Gate-voltage studies of discrete electronic states in aluminum nanoparticles *Phys. Rev. Lett.* **78** 4087–90
[102] Cobden D H, Bockrath M, McEuen P L, Rinzler A G and Smalley R E 1998 Spin splitting and even–odd effects in carbon nanotubes *Phys. Rev. Lett.* **81** 681–4
[103] Cobden D H, Bockrath M, Chopra N G, Zettl A, McEuen P L, Rinzler A, Thess A and Smalley R E 1998 Transport spectroscopy of single-walled carbon nanotubes *Physica* B **251** 132–5
[104] Cronenwett S M, Oosterkamp T H and Kouwenhoven L P 1998 A tunable Kondo effect in quantum dots *Science* **281** 540–4
[105] Goldhaber-Gordon D, Shtrikman H, Mahalu D, Abusch-Magder D, Meirav U and Kastner M A 1998 Kondo effect in a single-electron transistor *Nature* **391** 156–9
[106] Nyga ringrd J, Cobden D H and Lindelof P E 2000 Kondo physics in carbon nanotubes *Nature* **408** 342–6
[107] Buitelaar M R, Nussbaumer T and Schönenberger C 2002 Quantum dot in the Kondo regime coupled to superconductors *Phys. Rev. Lett.* **89** 256801
[108] Pasupathy A N, Bialczak R C, Martinek J, Grose J E, Donev L A K, McEuen P L and Ralph D C 2004 The Kondo effect in the presence of ferromagnetism *Science* **306** 86–9
[109] Yu L H and Natelson D 2004 The Kondo effect in C60 single-molecule transistors *Nano Lett.* **4** 79–83
[110] Geim A K and Novoselov K S 2007 The rise of graphene *Nat. Mater.* **6** 183–91
[111] Hod O, Baer R and Rabani E 2004 Feasible nanometric magnetoresistance devices *J. Phys. Chem.* B **108** 14807
[112] Hod O, Rabani E and Baer R 2005 Magnetoresistance devices based on single-walled carbon nanotubes *J. Chem. Phys.* **123** 051103
[113] Hod O, Baer R and Rabani E 2005 A parallel electromagnetic molecular logic gate *J. Am. Chem. Soc.* **127** 1648
[114] Hod O, Baer R and Rabani E 2006 Inelastic effects in Aharonov–Bohm molecular interferometers *Phys. Rev. Lett.* **97** 266803
[115] Hod O, Rabani E and Baer R 2006 Magneto-resistance of nanoscale molecular devices *Acc. Chem. Res.* **39** 109–117
[116] Jackson J D 1999 *Classical Electrodynamics* (New York: Wiley)
[117] Fuhrer A, Luescher S, Ihn T, Heinzel T, Ensslin K, Wegscheider W and Bichler M 2001 Energy spectra of quantum rings *Nature* **413** 822
[118] Kittel C 1996 *Introduction to Solid State Physics* (New York: Wiley)
[119] Datta S 1995 *Electronic Transport in Mesoscopic Systems* (Cambridge: Cambridge University Press)
[120] Datta S 2004 Electrical resistance: an atomistic view *Nanotechnology* **15** S433–51
[121] Gefen Y, Imry Y and Azbel N Y 1984 Quantum oscillations and the Aharonov–Bohm effect for parallel resistors *Phys. Rev. Lett.* **52** 129
[122] Cahay M, Bandyopadhyay S and Grubin H L 1989 Two types of conductance minima in electrostatic Aharonov–Bohm conductance oscillations *Phys. Rev.* B **39** 12989
[123] Imry Y 2002 *Introduction to Mesoscopic Physics* 2nd edn (Oxford: Oxford University Press)
[124] Aharony A, Entin-Wohlman O and Imry Y 2003 Measuring the transmission phase of a quantum dot in a closed interferometer *Phys. Rev. Lett.* **90** 156802
[125] Benjamin C, Bandopadhyay S and Jayannavar A M 2002 Survival of $\phi_0/2$ periodicity in presence of incoherence in asymmetric Aharonov–Bohm rings *Solid State Commun.* **124** 331–4
[126] Jayannavar A M and Benjamin C 2002 Wave attenuation model for dephasing and measurement of conditional times *Pramana J. Phys.* **59** 385–95
[127] Aharony A, Entin-Wohlman O, Halperin B I and Imry Y 2002 Phase measurement in the mesoscopic Aharonov–Bohm interferometer *Phys. Rev.* B **66** 115311
[128] Vugalter G A, Das A K and Sorokin V A 2004 A charged particle on a ring in a magnetic field: quantum revivals *Eur. J. Phys.* **25** 157–70
[129] Zehnder L 1891 Ein neuer interferenzrefraktor *Z. Instrumentenkunde* **11** 275–85
[130] Mach L 1892 Über einen interferenzrefraktor *Z. Instrumentenkunde* **12** 89–93
[131] Martel R, Schmidt T, Shea H R, Hertel T and Avouris Ph 1998 Single- and multi-wall carbon nanotube field-effect transistors *Appl. Phys. Lett.* **73** 2447
[132] Bachtold A, Hadley P, Nakanishi T and Dekker C 2001 Logic circuits with carbon nanotube transistors *Science* **294** 1317
[133] Javey A, Guo J, Wang Q, Lundstrom M and Dai H 2003 Ballistic carbon nanotube field-effect transistors *Nature* **424** 654
[134] Wu C H and Ramamurthy D 2002 Logic functions of three-terminal quantum resistor networks for electron wave computing *Phys. Rev.* B **65** 075313
[135] Ramamurthy D and Wu C H 2002 Four-terminal quantum resistor network for electron-wave computing *Phys. Rev.* B **66** 115307
[136] Ionicioiu R and D'Amico I 2003 Mesoscopic Stern–Gerlach device to polarize spin currents *Phys. Rev.* B **67** 041307
[137] Yi J and Cuniberti G 2003 A three terminal ring interferometer logic gate *Ann. New York Acad. Sci.* **1006** 306
[138] Margulis V A and Pyataev M 2004 Fano resonances in a three-terminal nanodevice *J. Phys.: Condens. Matter* **16** 4315
[139] Shelykh I A, Galkin N G and Bagraev N T 2005 Quantum splitter controlled by rasha spin–orbit coupling *Phys. Rev.* B **72** 235316
[140] Szafran B and Peeters F M 2005 Lorentz-force-induced asymmetry in the Aharonov–Bohm effect in a three-terminal semiconductor quantum ring *Europhys. Lett.* **70** 810–6
[141] Leturcq R, Schmid L, Ensslin K, Meir Y, Driscoll D C and Gossard A C 2005 Probing the Kondo density of states in a three-terminal quantum ring *Phys. Rev. Lett.* **95** 126603
[142] Földi P, Kálmán O, Benedict M G and Peeters F M 2006 Quantum rings as electron spin beam splitters *Phys. Rev.* B **73** 155325
[143] Leturcq R, Schmid L, Ihn T, Ensslin K, Driscoll D C and Gossard A C 2006 Asymmetries of the conductance matrix in a three-terminal quantum ring in the coulomb blockade regime *Physica* E **34** 445–8
[144] Joe Y S, Hedin E R and Satanin A M 2007 Manipulation of resonances in an open three-terminal interferometer with an embedded quantum dot *Phys. Rev.* B **76** 085419
[145] Cohen G, Hod O and Rabani E 2007 Constructing spin interference devices from nanometric rings *Phys. Rev.* B **76** 235120
[146] Onsager L 1931 Reciprocal relations in irreversible processes. II *Phys. Rev.* **38** 2265–79
[147] Büttiker M 1986 Four-terminal phase-coherent conductance *Phys. Rev. Lett.* **57** 1761–4

[148] Entin-Wohlman O, Aharony A, Imry Y, Levinson Y and Schiller A 2002 Broken unitarity and phase measurements in Aharonov–Bohm interferometers *Phys. Rev. Lett.* **88** 166801

[149] Palm T and Thylén L 1996 Designing logic functions using an electron waveguide *y*-branch switch *J. Appl. Phys.* **79** 8076

[150] Keldysh L V 1965 Diagram technique for nonequilibrium processes *Sov. Phys.—JETP* **20** 1018

[151] Kadanoff L P and Baym G 1962 *Quantum Statistical Mechanics. Green's Function Methods in Equilibrium and Nonequilibrium Problems* (Reading, MA: Benjamin)

[152] Wagner M 1991 Expansions of nonequilibrium Green's functions *Phys. Rev.* B **44** 6104–17

[153] Damle P S, Ghosh A W and Datta S 2001 Unified description of molecular conduction: from molecules to metallic wires *Phys. Rev.* B **64** 201403

[154] Galperin M and Nitzan A 2003 NEGF-HF method in molecular junction property calculations *Mol. Electron. III; Ann. New York Acad. Sci.* **1006** 48–67

[155] Ghosh A W, Damle P, Datta S and Nitzan A 2004 Molecular electronics: theory and device prospects *MRS Bull.* **29** 391–5

[156] Galperin M, Ratner M A and Nitzan A 2007 Molecular transport junctions: vibrational effects *J. Phys.: Condens. Matter* **19** 103201

[157] Todorov T N, Briggs G A D and Sutton A P 1993 Elastic quantum transport through small structures *J. Phys.: Condens. Matter* **5** 2389–406

[158] Pleutin S, Grabert H, Ingold G L and Nitzan A 2003 The electrostatic potential profile along a biased molecular wire: a model quantum-mechanical calculation *J. Chem. Phys.* **118** 3756–63

[159] Landauer R 1957 Spatial variation of currents and fields due to localized scatterers in metallic conduction *IBM J. Res. Dev.* **1** 223–31

[160] Xue Y, Datta S and Ratner M A 2002 First-principles based matrix Green's function approach to molecular electronic devices: general formalism *Chem. Phys.* **281** 151–70

[161] Paulsson M 2002 Non equilibrium Green's functions for dummies: introduction to the one particle NEGF equations *Preprint* cond-mat/0210519 v1

[162] López Sancho M P, López Sancho J M and Rubio J 1984 Quick iterative scheme for the calculation of transfer matrices: application to mo (100) *J. Phys. F: Met. Phys.* **14** 1205–15

[163] López Sancho M P, López Sancho J M and Rubio J 1985 Highly convergent schemes for the calculation of bulk and surface Green functions *J. Phys. F: Met. Phys.* **15** 851–8

[164] Nardelli M B 1999 Electronic transport in extended systems: application to carbon nanotubes *Phys. Rev.* B **60** 7828–33

[165] Galperin M, Ratner M A and Nitzan A 2004 Inelastic electron tunneling spectroscopy in molecular junctions: peaks and dips *J. Chem. Phys.* **121** 11965–79

[166] Neuhauser D and Baer M 1989 The time-dependent Schrödinger equation: application of absorbing boundary conditions *J. Chem. Phys.* **90** 4351–5

[167] Seideman T and Miller W H 1992 Quantum mechanical reaction probabilities via a discrete variable representation–absorbing boundary condition Green's function *J. Chem. Phys.* **97** 2499–514

[168] Baer R and Neuhauser D 2002 Phase coherent electronics: a molecular switch based on quantum interference *J. Am. Chem. Soc.* **124** 4200

[169] Riss U V and Meyer H D 1996 Investigation on the reflection and transmission properties of complex absorbing potentials *J. Chem. Phys.* **105** 1409–19

[170] Nitta J, Meijer F E and Takayanagi H 1999 Spin-interference device *Appl. Phys. Lett.* **75** 695–7

[171] Frustaglia D, Hentschel M and Richter K 2001 Quantum transport in nonuniform magnetic fields: Aharonov–Bohm ring as a spin switch *Phys. Rev. Lett.* **87** 256602

[172] Ionicioiu R and D'Amico I 2003 Stern–Gerlach device to polarize spin currents *Phys. Rev.* B **67** 041307

[173] Popp M, Frustaglia D and Richter K 2003 Spin filter effects in mesoscopic ring structures *Nanotechnology* **14** 347–51

[174] Molnar B, Peeters F M and Vasilopoulos P 2004 Spin-dependent magnetotransport through a ring due to spin–orbit interaction *Phys. Rev.* B **69** 155335

[175] Hentschel M, Schomerus H, Frustaglia D and Richter K 2004 Aharonov–Bohm physics with spin. I. Geometric phases in one-dimensional ballistic rings *Phys. Rev.* B **69** 155326

[176] Frustaglia D, Hentschel M and Richter K 2004 Aharonov–Bohm physics with spin. II. Spin-flip effects in two dimensional ballistic systems *Phys. Rev.* B **69** 155327

[177] Frustaglia D and Richter K 2004 Spin interference effects in ring conductor subject to Rashba coupling *Phys. Rev.* B **69** 235310

[178] Aeberhard U, Wakabayashi K and Sigrist M 2005 Effect of spin–orbit coupling on zero-conductance resonances in asymmetrically coupled one-dimensional rings *Phys. Rev.* B **72** 075328

[179] Wang X F and Vasilopoulos P 2005 Spin-dependent magnetotransport through a mesoscopic ring in the presence of spin–orbit interaction *Phys. Rev.* B **72** 165336

[180] Földi P, Molnár B, Benedict M G and Peeters F M 2005 Spintronic single-qubit gate based on a quantum ring with spin–orbit interaction *Phys. Rev.* B **71** 033309

[181] Molnar B, Vasilopoulos P and Peeters F M 2005 Magnetoconductance through a chain of rings with or without periodically modulated spin–orbit interaction strength and magnetic field *Phys. Rev.* B **72** 075330

[182] Ramaglia V M, Cataudella V, De Filippis G and Perroni C A 2006 Ballistic transport in one-dimensional loops with Rashba and Dresselhaus spin–orbit coupling *Phys. Rev.* B **73** 155328

[183] Rashba E I 1960 Properties of semiconductors with an extremum loop.1. cyclotron and combinational resonance in a magnetic field perpendicular to the plane of the loop *Sov. Phys.—Solid State* **2** 1109–22

[184] Dresselhaus G 1955 Spin–orbit coupling effects in zinc blende structures *Phys. Rev.* **100** 580–6

[185] Hoffmann R 1963 An extended Huckel theory. I. Hydrocarbons *J. Chem. Phys.* **39** 1397

[186] Cohen-Tannoudji C, Diu B and Laloë F 1977 *Quantum Mechanics* (New York: Wiley)

[187] Slater J C 1930 Atomic shielding constants *Phys. Rev.* **36** 57–64

[188] Pople J A and Beveridge D L 1970 *Approximate Molecular Orbital Theory* (New York: McGraw-Hill)

[189] London F 1937 Theorie quantique des courants interatomiques dans les combinaisons aromatique *J. Phys. Radium* **8** 397–409

[190] Pople J A 1962 Molecular-orbital theory of diamagnetism. I. An approximate LCAO scheme *J. Chem. Phys.* **37** 53–9

[191] Guseinov I I 1970 Analytical evaluation of two-centre Coulomb, hybrid and one-electron integrals for Slater-type orbitals *J. Phys. B: At. Mol. Phys.* **3** 1399–412

[192] Guseinov I I 1985 Evaluation of two-center overlap and nuclear-attraction integrals for Slater-type orbitals *Phys. Rev.* A **32** 1864–6

[193] Guseinov I I, Özmen A, Atav Ü and Yüksel H 1998 Computation of overlap integrals over Slater-type orbitals using auxiliary functions *Int. J. Quantum Chem.* **67** 199–204

[194] Guseinov I I and Mamedov B A 1999 Computation of molecular integrals over Slater type orbitals. I. Calculations of overlap integrals using recurrence relations *J. Mol. Struct. (Theochem)* **465** 1–6

[195] Guseinov I I 2003 Response to the comment: on the computation of molecular auxiliary functions *an* and *bn* *Pramana J. Phys.* **61** C781

[196] Hod O 2005 Molecular nano-electronic devices based on Aharonov–Bohm interferometry *PhD Thesis* Tel Aviv University

[197] Collins G P 1993 STM rounds up electron waves at the QM corral *Phys. Today* **46** 17–9

[198] Crommie M F, Lutz C P and Eigler D M 1993 Confinement of electrons to quantum corrals on a metal surface *Science* **262** 218–20

[199] Manoharan H C, Lutz C P and Eigler D M 2000 Quantum mirages formed by coherent projection of electronic structure *Nature* **403** 512–5

[200] Nazin G V, Qiu X H and Ho W 2003 Visualization and spectroscopy of a metal–molecule–metal bridge *Science* **302** 77

[201] Iijima S 1991 Helical microtubules of graphitic carbon *Nature* **354** 56

[202] Collins P G and Avouris P 2000 Nanotubes for electronics *Sci. Am.* **283** (December) 62

[203] Fuhrer M S *et al* 2000 Crossed nanotube junctions *Science* **288** 494

[204] Zhou C, Kong J, Yenilmez E and Dai H 2000 Modulated chemical doping of individual carbon nanotubes *Science* **290** 1552

[205] Rueckes T, Kim K, Joselevich E, Tseng G Y, Cheung C-L and Lieber C M 2000 Carbon nanotube-based nonvolatile random access memory for molecular computing *Science* **289** 94

[206] Bockrath M, Liang W, Bozovic D, Hafner J H, Lieber C M, Tinkham M and Park H 2001 Resonant electron scattering by defects in single-walled carbon nanotubes *Science* **291** 283

[207] Treboux G, Lapstun P and Silverbrook K 1999 Conductance in nanotube *y*-junctions *Chem. Phys. Lett.* **306** 402

[208] Léonard F and Tersoff J 2000 Negative differential resistance in nanotube devices *Phys. Rev. Lett.* **85** 4767

[209] Andriotis A N, Menon M, Srivastava D and Chernozatonskii L 2001 Rectification properties of carbon nanotube '*y*-junctions' *Phys. Rev. Lett.* **87** 66802

[210] Ajiki H and Ando T 1994 Aharonov–Bohm effect in carbon nanotubes *Physica* B **201** 349–52

[211] Lin M F 1998 Magnetic properties of toroidal carbon nanotubes *J. Phys. Soc. Japan* **67** 1094–7

[212] Bachtold A, Strunk C, Salvetat J-P, Bonard J-M, Forro L, Nussbaumer T and Schonenberger C 1999 Aharonov–Bohm oscillations in carbon nanotubes *Nature* **397** 673–5

[213] Fujiwara A, Tomiyama K, Suematsu H, Yumura M and Uchida K 1999 Quantum interference of electrons in multiwall carbon nanotubes *Phys. Rev.* B **60** 13492–6

[214] Ando T 2000 Theory of transport in carbon nanotubes *Semicond. Sci. Technol.* **15** R13–27

[215] Roche S, Dresselhaus G, Dresselhaus M S and Saito R 2000 Aharonov–Bohm spectral features and coherence lengths in carbon nanotubes *Phys. Rev.* B **62** 16092–9

[216] Zaric S, Ostojic G N, Kono J, Shavey J, Moore V C, Strano M S, Hauge R H, Smalley R E and Wei X 2004 Optical signatures of the Aharonov–Bohm effect in single-walled carbon nanotubes *Science* **304** 1129

[217] Coskun U C, Wei T-C, Vishveshwara S, Goldbart P M and Bezryadin A 2004 h/e magnetic flux modulation of the energy gap in nanotube quantum dots *Science* **304** 1132

[218] Cao J, Wang Q, Rolandi M and Dai H 2004 Aharonov–Bohm interference and beating in single-walled carbon-nanotube interferometers *Phys. Rev. Lett.* **93** 216803

[219] Cao J, Wang Q and Dai H 2005 Electron transport in very clean, as-grown suspended carbon nanotubes *Nat. Mater.* **4** 745–9

[220] Charlier J C, Blase X and Roche S 2007 Electronic and transport properties of nanotubes *Rev. Mod. Phys.* **79** 677–732

[221] Deshmukh M M, Prieto A L, Gu Q and Park H 2003 Fabrication of asymmetric electrode pairs with nanometer separation made of two distinct metals *Nano Lett.* **3** 1383–5

[222] Xie F Q, Nittler L, Obermair C and Schimmel T 2004 Gate-controlled atomic quantum switch *Phys. Rev. Lett.* **93** 128303

[223] Biercuk M J, Mason N, Martin J, Yacoby A and Marcus C M 2005 Anomalous conductance quantization in carbon nanotubes *Phys. Rev. Lett.* **94** 026801

[224] Javey A, Qi P, Wang Q and Dai H 2004 Ten-to 50-nm-long quasi-ballistic carbon nanotube devices obtained without complex lithography *Proc. Natl Acad. Sci.* **101** 13408–10

[225] Staab H A and Diederich F 1978 Benzenoid versus annulenoid aromaticity: synthesis and properties of kekulene *Angew. Chem. Int. Edn Engl.* **17** 372–4

[226] Staab H A and Diederich F 1983 Cycloarenes, a new class of aromatic compounds, I. Synthesis of kekulene *Chem. Ber.* **116** 3487–503

[227] Staab H A, Diederich F, Krieger C and Schweitzer D 1983 Cycloarenes, a new class of aromatic compounds, II. Molecular structure and spectroscopic properties of kekulene *Chem. Ber.* **116** 3504–12

[228] Cioslowski J, O'connor P B and Fleischmann E D 1991 Is superbenzene superaromatic? *J. Am. Chem. Soc.* **113** 1086–9

[229] Aihara J 1992 Is superaromaticity a fact or an artifact? the kekulene problem *J. Am. Chem. Soc.* **114** 865–8

[230] Steiner E, Fowler P W, Jenneskens L W and Acocella A 2001 Visualisation of counter-rotating ring currents in kekulene *Chem. Commun.* 659–60

[231] Hajgató B and Ohno K 2004 Novel series of giant polycyclic aromatic hydrocarbons: electronic structure and aromaticity *Chem. Phys. Lett.* **385** 512–8

[232] Ezawa M 2006 Peculiar width dependence of the electronic properties of carbon nanoribbons *Phys. Rev.* B **73** 045432

[233] Son Y-W, Cohen M L and Louie S G 2006 Half-metallic graphene nanoribbons *Nature* **444** 347–9

[234] Son Y-W, Cohen M L and Louie S G 2006 Energy gaps in graphene nanoribbons *Phys. Rev. Lett.* **97** 216803

[235] Barone V, Hod O and Scuseria G E 2006 Electronic structure and stability of semiconducting graphene nanoribbons *Nano Lett.* **6** 2748

[236] Hod O, Barone V, Peralta J E and Scuseria G E 2007 Enhanced half-metallicity in edge-oxidized zigzag graphene nanoribbons *Nano Lett.* **7** 2295–9

[237] Castro-Neto A H, Guinea F, Peres N M R, Novoselov K S and Geim A K 2007 The electronic properties of graphene *Preprint* 0709.1163

[238] Ness H and Fisher A J 1999 Quantum inelastic conductance through molecular wires *Phys. Rev. Lett.* **83** 452–5

[239] Segal D and Nitzan A 2002 Conduction in molecular junctions: inelastic effects *Chem. Phys.* **281** 235–56

[240] Montgomery M J, Todorov T N and Sutton A P 2002 Power dissipation in nanoscale conductors *J. Phys.: Condens. Matter* **14** 5377–90

[241] Flensberg K 2003 Tunneling broadening of vibrational sidebands in molecular transistors *Phys. Rev.* B **68** 205323

[242] Petrov E G, May V and Hanggi P 2004 Spin-boson description of electron transmission through a molecular wire *Chem. Phys.* **296** 251–66

[243] Mii T, Tikhodeev S G and Ueba H 2003 Spectral features of inelastic electron transport via a localized state *Phys. Rev.* B **68** 205406

[244] Mitra A, Aleiner I and Millis A J 2004 Phonon effects in molecular transistors: quantal and classical treatment *Phys. Rev.* B **69** 245302

[245] Paulsson M, Frederiksen T and Brandybge M 2005 Modeling inelastic phonon scattering in atomic- and molecular-wire junctions *Phys. Rev.* B **72** 201101(R)

[246] Galperin M, Nitzan A and Ratner M A 2006 Inelastic tunneling effects on noise properties of molecular junctions *Phys. Rev.* B **74** 075326
[247] Mühlbacher L and Rabani E 2008 Real-time path integral approach to nonequilibrium many-body quantum systems *Phys. Rev. Lett.* **100** 176403
[248] Wang H and Thoss M, unpublished
[249] Guinea F 2002 Aharonov–Bohm oscillations of a particle coupled to dissipative environments *Phys. Rev.* B **65** 205317
[250] Ludwig T and Mirlin A D 2004 Interaction-induced dephasing of Aharonov–Bohm oscillations *Phys. Rev.* B **69** 193306
[251] Jauho A P, Wingreen N S and Meir Y 1994 Time-dependent transport in interacting and noninteracting resonant-tunneling systems *Phys. Rev.* B **50** 5528
[252] Stipe B C, Rezaei M A and Ho W 1998 Single-molecule vibrational spectroscopy and microscopy *Science* **280** 1732–5
[253] Thijssen W H A, Djukic D, Otte A F, Bremmer R H and van Ruitenbeek J M 2006 Vibrationally induced two-level systems in single-molecule junctions *Phys. Rev. Lett.* **97** 226806
[254] Wu C H and Mahler G 1991 Quantum network theory of transport with application to the generalized Aharonov–Bohm effect in metals and semiconductors *Phys. Rev.* B **43** 5012–23
[255] Wu C H and Ramamurthy D 2002 Logic functions of three-terminal quantum resistor networks for electron wave computing *Phys. Rev.* B **65** 075313
[256] Silva A, Oreg Y and Gefen Y 2002 Sign of quantum dot–lead matrix elements: the effect of transport versus spectral properties *Phys. Rev.* B **66** 195316
[257] Ryndyk D A, Gutierrez R, Song B and Cuniberti G 2008 Green function techniques in the treatment of quantum transport at the molecular scale *Preprint* 0805.0628v1